



Reaction mechanism reduction for ethylene-fueled supersonic combustion CFD

Kan Kobayashi¹ · Sadatake Tomioka¹ · Masahiro Takahashi¹ · Masatoshi Kodera¹

Received: 18 October 2022 / Revised: 15 January 2023 / Accepted: 2 February 2023 / Published online: 27 February 2023
© The Author(s) 2023

Abstract

CHEMKIN-Pro was used to build a custom-made reduced reaction mechanism for a 3D simulation of C₂H₄/Air reaction in a supersonic combustion ramjet (scramjet) combustor for the JAXA S-520-RD1 flight test performed on 24 July 2022. It was also attempted to reproduce the effect of unavoidable H₂O vitiation in the facility (ground) test on combustion characteristics. USC Mech II (a 111-species mechanism) was applied as the master mechanism. First, 1D simulation was conducted by applying a plug flow reactor model; 34-, 23-, 20-, 18-, and 19-species mechanisms were suggested as candidates for reduced mechanism. Then, 0D ignition delay simulation by applying a perfectly stirred reactor model by CHEMKIN-Pro, 2D reacting flow simulation by CRUNCH CFD, and 3D reacting flow simulation by RANS were performed to select the most suitable reduced mechanism. The 20-species (96-elementary-reactions) mechanism consisted of H₂, O₂, N₂, H₂O, CO₂, CO, H, O, OH, HO₂, CH₂, CH₂^{*}, CH₃, HCO, CH₂O, CH₃O, C₂H₂, C₂H₃, C₂H₄, and CH₂CHO and was selected as the best-reduced reaction mechanism for C₂H₄-fueled 3D simulation under the flight and facility conditions corresponding to the RD1 flight test.

Keywords Propulsion · Scramjet engine · Flight test · Combustion simulation · Reaction mechanism

1 Introduction

On 24 July 2022, the Japan Aerospace Exploration Agency (JAXA) launched a sounding rocket, S-520-RD1, to demonstrate C₂H₄-fueled supersonic combustion under Mach 5.5–6 and 25–100 kPa in dynamic pressure [1] (Fig. 1). The primary objective of the RD1 project is to build a 3D simulation tool that can reproduce both facility (or ground) and flight test data because facility test data includes the effect of unavoidable H₂O vitiation (or contamination) on combustion characteristics [2]. The project aims to reproduce the flight test data using a tool tuned to reproduce the facility test data. Once such a tool is built, flight test data under any

conditions can be inferred from the corresponding facility test data and the tool without needing a flight test. Using the flight test data obtained in July 2022 [3] and the corresponding facility test data obtained in October 2022 [4], validation and tuning of the tool are ongoing. Note that a reaction mechanism is one of the tuning parameters of the tool. Since a scramjet engine is an air-breathing engine, and C₂H₄ was the fuel for the RD1 flight test, a C₂H₄/Air reaction mechanism is required. Although some reduced reaction mechanisms applicable to C₂H₄/Air reaction simulations have been proposed (for example, a 31-species model by Zambon et al. [5], the 3-step (7 species) model by Mawid et al. [6], and the modified 3-step models by Eklund et al. [7] and Hassan et al. [8]), the reproducibility of the combustion characteristics changes depending on the simulation target and conditions focused on. Therefore, finding a versatile reaction mechanism from existing reduced mechanisms is generally difficult.

In the present study, some reductions of the detailed C₂H₄/air reaction mechanism, including more than 100 chemical species, were attempted under the specific conditions for the flight test, using the commercially available software CHEMKIN-Pro [9]. Due to the limitations of 3D simulation, the target number of species after reduction is

✉ Kan Kobayashi
kobayashi.kan@jaxa.jp

Sadatake Tomioka
tomioka.sadatake@jaxa.jp

Masahiro Takahashi
takahashi.masahiro@jaxa.jp

Masatoshi Kodera
koderam.masatoshi@jaxa.jp

¹ Japan Aerospace Exploration Agency (JAXA), Kakuda, Miyagi 981-1525, Japan

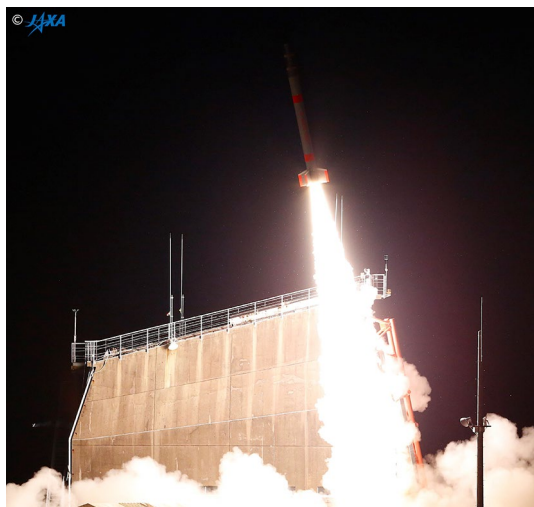


Fig. 1 S-520-RD1 launched on 24 July 2022

around 20. This study aims to establish a methodology to obtain a custom-made reaction mechanism for a specific target rather than constructing a versatile reaction mechanism applicable to many targets.

2 Simplification of target flow field to 1D simulation

In reducing the reaction mechanism in CHEMKIN-Pro, the user specifies the simulation target and conditions of interest while referring to the results obtained from the detailed reaction mechanism, also specified by the user. The number of chemical species is gradually reduced while monitoring to minimize deviations from the results with a detailed reaction mechanism, namely, a master mechanism. In other words, the simulation target applied to this work must be a simulation to which the detailed reaction mechanism can be applied. Therefore, even if the goal is a 3D reacting flow simulation, it must first be replaced with a lower-dimensional simulation. The simulation target of the present study is the 3D flow field with reaction in the flight model combustor. Thus, this 3D flow field in the combustor is replaced with a 1D flow field in this section.

Figure 2a is the conceptual structure of the flight model. The airflow enters the opening in the front, is compressed by a ramp compression unit (inlet) with a length of 0.38 m, and passes through a constant cross-sectional area duct (isolator) with a length of 0.2 m. It flows into the 0.3 m constant cross-sectional area combustor. After that, it flows out the exhaust duct through the diverging combustor with a length of 0.6 m.

Figure 2b shows the conceptual design of the combustor section with a length of 0.3 m + 0.6 m. The cavity flame holder in the constant cross-sectional area combustor

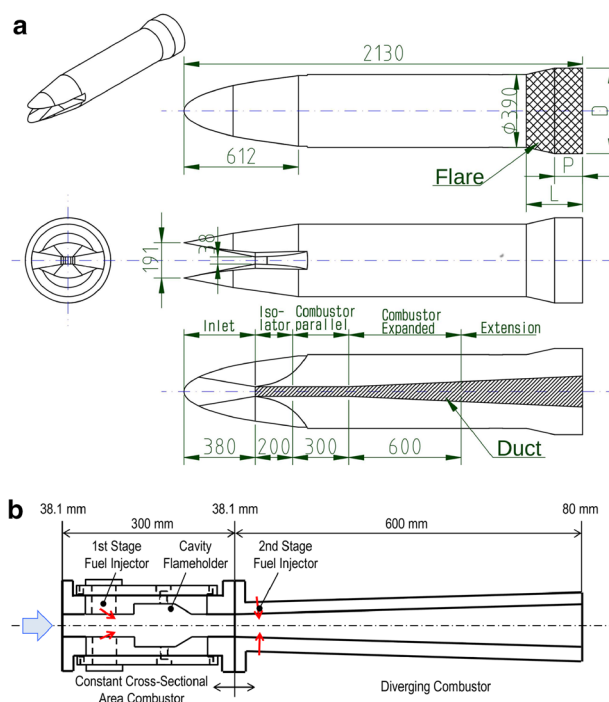


Fig. 2 **a** Conceptual structure of the flight model. **b** Conceptual design of the combustor section

ensures enough residence time, longer than the reaction time, by circulating a part of the high-speed air and fuel flow to ensure ignition and flame holding. The combustor has two sets of fuel injectors. The first- and second-stage fuel injectors are in the constant cross-sectional area combustor and the diverging combustor, respectively. The background of this two-stage fuel injection system will be mentioned later.

Note that Fig. 2a, b are from the initial study (so they are called “conceptual”). The 1D and 2D simulations in the present study were performed with them. They differ from those in the actual flight test, shown in Ref. [1, 3]. For example, the diverging combustor entrance was directly connected to the isolator exit (no constant cross-sectional area combustor), so cavities were included in the diverging combustor for the flight model. In addition, a diverging angle was changed from 2° (for the initial study) to 1.3° (for flight) on each side.

The present study focuses on “facility conditions” and “flight conditions.” The primary experimental method of scramjet research is facility (ground) tests. The air must be heated before accelerating it to supersonic speed to impart a high enthalpy to the airflow. In particular, combustion heat is used to heat the airflow to perform the relatively high Mach number tests, which requires a relatively high total temperature of airflow. For example, the RamJet engine Test Facility (RJTF) in the JAXA Kakuda Space Center uses H_2 -lean combustion [2], which generates H_2O as the combustion product. The O_2 mole fraction in the hot airflow

generated is controlled to 0.21 by adding make-up O_2 , but H_2O vitiation, which affects the combustion characteristics in the engine, is unavoidable. In actual flight, however, air-flow entering the engine consists of pure air. In the present study, the former (with H_2O vitiation) and latter (without H_2O vitiation) conditions are designated as “facility” and “flight” conditions, respectively.

To detect a difference in combustion characteristics between facility and flight conditions, it is desirable to burn in an environment where the progress of the reaction is moderately slow, that is, in an appropriate low-temperature and pressure environment. Thus, it is required to inject fuel into the diverging combustor in which the flow path expands, and the static temperature and pressure gradually decrease. However, the airflow at the diverging combustor entrance is not so high in static temperature and pressure that C_2H_4 combustion can be achieved. Therefore, a part of the fuel needs to be burned in the constant cross-sectional area combustor, and the static temperature and pressure of the airflow at the diverging combustor entrance are increased to some extent. Based on this, it was decided to adopt a two-stage fuel injection system, the first-stage injection from the constant cross-sectional area combustor and the second-stage injection from the diverging combustor. Note that the optimal equivalence ratio is 0.25 in each stage (total equivalence ratio is 0.5), and the optimal diverging angle of the diverging combustor is 2° on each side (total diverging angle is 4°) in this combustor.

The primary purpose of the 3D reacting flow simulation is to reproduce the difference in combustion characteristics, especially in the diverging combustor, between flight and facility conditions. Therefore, the simulation applied to the reaction mechanism reduction must approximate the flow field in the diverging combustor in 1D. The present study considers that C_2H_4 with an equivalence ratio of 0.25 injected from the first stage and air are premixed. The equilibrium combustion gas that has reached the equilibrium state (O_2 remains due to C_2H_4 -lean combustion) flows into the diverging combustor. After the combustion gas flows into the diverging combustor, the flow field changes (static temperature and pressure decrease) according to the expansion of the flow path up to the second-stage fuel injection location. At the second-stage fuel injection location, C_2H_4 with an equivalence ratio of 0.25 and the equilibrium combustion gas at that location mix instantly, and the reaction starts from that location. From the above, in the reduction of the reaction mechanism that also needs to apply the detailed reaction mechanism, the cross section is homogeneous at each location in the flow direction (x direction), and the “plug flow” in which the state in the cross section including the cross-sectional area changes in the flow direction was adopted. After applying the plug flow reactor model, a 1D reacting flow simulation is performed within the area

from the second-stage fuel injection location to the diverging combustor exit.

3 Reaction mechanism reduction by CHEMKIN-Pro with 1D simulation

3.1 1D simulation by “plug flow reactor” model

In flight and facility conditions, the most suitable target for measuring the difference in combustion in the diverging combustor is the static pressure distribution for ease of measurement. The static pressure distribution is also used to evaluate thrust performance, which is particularly important in engine performance. Therefore, the present study emphasizes the static pressure distribution. Also, in reducing the reaction mechanism (described later), the paper focuses on the static pressure distribution, considering the simulation results obtained by the detailed reaction mechanism. The reduction is advanced so that this can be accurately reproduced.

This section describes a detailed reaction mechanism before reducing the reaction mechanism. Then, 1D reacting flow simulation using a plug flow reactor (PFR) model was performed to find the optimum conditions (i.e., the second-stage fuel injection location where the difference in static pressure distribution between flight and facility conditions is most clearly detected). The simulation conditions were fixed at the first-stage equivalence ratio of 0.25, the second-stage equivalence ratio of 0.25 (0.5 in total), and a diverging angle of 2° on each side (4° in total). The second-stage fuel injection location, where the 1D reacting flow simulation starts, was changed to 0, 0.09, 0.18, and 0.27 m from the diverging combustor entrance. The various distributions under flight and facility conditions are examined here. The USC Mech II by Wang et al. [10] (111 chemical species, 770 elementary reactions), which can reproduce the ignition delay obtained in the shock tube test [11], was adopted as a detailed reaction mechanism. Wang et al. [10] provide validation results with the USC Mech II. For example, ignition delay for C_2H_4 was validated under 0.5–2.0 equivalence ratio, 70–300 kPa, and 1250–2380 K.

Figure 3 shows the input parameter calculation process for 1D simulation. The flight Mach number was set to 6, and the ambient air conditions, namely the static pressure and temperature, were set to 3.54 kPa and 217 K, respectively. These parameters, shown in the yellow box in Fig. 3, are common to the flight and facility conditions in 1D simulation. Between flight and facility conditions, the input parameters for 1D simulation were obtained because the specific heat ratios (1.40 for flight, 1.38 for the facility) and the molecular weights of the airflow (28.8 g/mol for flight, 27.1 g/mol for the facility) were different due to H_2O vitiation under

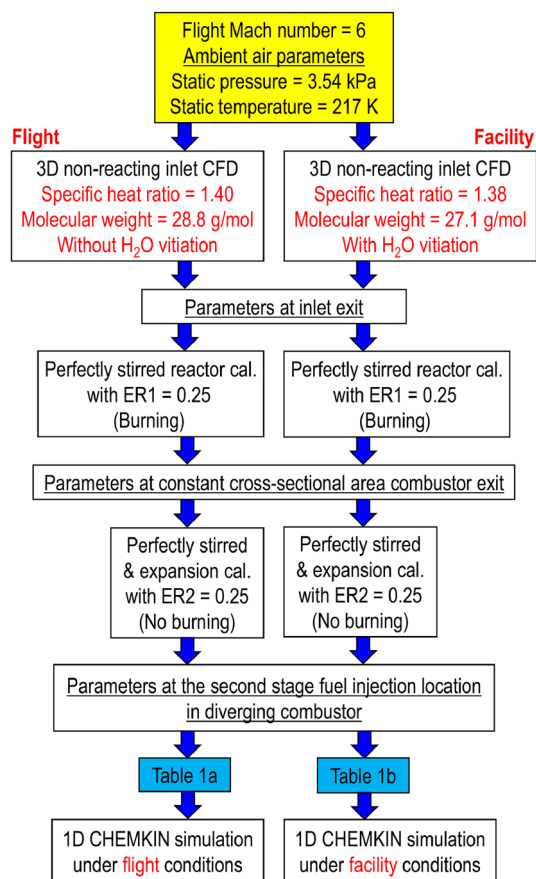


Fig. 3 Input parameter calculation process for 1D simulation

facility conditions. First, the Mach number, static pressure, and static temperature at the inlet exit (i.e., the entrance of the constant cross-sectional area combustor) were calculated using the 3D non-reacting flow simulation for the inlet. Second, from the parameters at the inlet exit and the first-stage fuel mass flow rate, corresponding to a 0.25 equivalence ratio, equilibrium calculations were performed assuming a perfectly stirred reactor to obtain the Mach number, the static pressure, the static temperature, and the composition at the injection location of the second-stage fuel (i.e., the starting position for 1D PFR analysis). As mentioned above, the location of the second-stage fuel injection was changed in the diverging combustor for the present study. Note that the Mach number, the static pressure, the static temperature, and the composition were different among these locations due to channel expansion. Third, from these parameters at the second-stage fuel injection location and the second-stage fuel mass flow rate corresponding to a 0.25 equivalence ratio without combustion (only perfectly stirred), the parameters applied to the 1D PFR analysis were obtained as shown in Table 1a, b for flight and facility conditions, respectively. Differences in H₂O mole fraction due to H₂O vitiation in facility conditions can be seen in these tables.

Table 1 Input parameters for 1D simulation for (a) flight conditions, (b) facility conditions

| | 0 m | 0.09 m | 0.18 m | 0.27 m |
|--------------------------------|-----------|-----------|-----------|-----------|
| (a) Flight conditions | | | | |
| Mass flow rate, g/s | 564.6 | | | |
| Static pressure, kPa | 106.0 | 79.1 | 62.7 | 51.4 |
| Static temperature, K | 1567.2 | 1470.6 | 1398.8 | 1338.8 |
| Mach number | 1.634 | 1.819 | 1.960 | 2.078 |
| Mole fraction | | | | |
| C ₂ H ₄ | 1.688E-02 | 1.687E-02 | 1.687E-02 | 1.686E-02 |
| CO | 1.090E-06 | 3.070E-07 | 1.060E-07 | 3.970E-08 |
| CO ₂ | 3.405E-02 | 3.403E-02 | 3.402E-02 | 3.401E-02 |
| H | 2.290E-08 | 4.890E-09 | 1.340E-09 | 4.060E-10 |
| H ₂ | 3.780E-07 | 1.240E-07 | 4.870E-08 | 2.050E-08 |
| H ₂ O | 3.372E-02 | 3.372E-02 | 3.372E-02 | 3.372E-02 |
| N ₂ | 7.550E-01 | 7.549E-01 | 7.548E-01 | 7.548E-01 |
| O | 3.690E-06 | 1.190E-06 | 4.600E-07 | 1.910E-07 |
| O ₂ | 1.511E-01 | 1.513E-01 | 1.515E-01 | 1.515E-01 |
| OH | 7.440E-05 | 3.530E-05 | 1.890E-05 | 1.060E-05 |
| (b) Facility conditions | | | | |
| Mass flow rate, g/s | 551.1 | | | |
| Static pressure, kPa | 102.0 | 77.0 | 61.4 | 50.6 |
| Static temperature, K | 1493.85 | 1409.96 | 1346.64 | 1293.11 |
| Mach number | 1.683 | 1.856 | 1.990 | 2.103 |
| Mole fraction | | | | |
| C ₂ H ₄ | 1.687E-02 | 1.686E-02 | 1.686E-02 | 1.686E-02 |
| CO | 3.860E-07 | 1.160E-07 | 4.200E-08 | 1.630E-08 |
| CO ₂ | 3.396E-02 | 3.395E-02 | 3.394E-02 | 3.394E-02 |
| H | 1.570E-08 | 3.640E-09 | 1.060E-09 | 3.380E-10 |
| H ₂ | 9.310E-07 | 3.230E-07 | 1.330E-07 | 5.810E-08 |
| H ₂ O | 2.091E-01 | 2.091E-01 | 2.090E-01 | 2.090E-01 |
| N ₂ | 5.817E-01 | 5.816E-01 | 5.816E-01 | 5.816E-01 |
| O | 1.450E-06 | 4.930E-07 | 1.990E-07 | 8.600E-08 |
| O ₂ | 1.513E-01 | 1.514E-01 | 1.516E-01 | 1.516E-01 |
| OH | 1.014E-04 | 5.000E-05 | 2.760E-05 | 1.590E-05 |

Figure 4a shows the static pressure distributions. The up arrows in the figure indicate the position of the second-stage fuel injection. When the second-stage fuel injection location is $x = 0$ and 0.09 m, the peak pressure locations of the flight and facility conditions are almost the same. The static temperature and pressure are relatively high at these locations, and the reaction is too fast to detect the difference. When the second-stage fuel injection location is $x = 0.18$ m, there is an increase in static pressure due to combustion, and there is a difference in the peak locations for the flight and facility

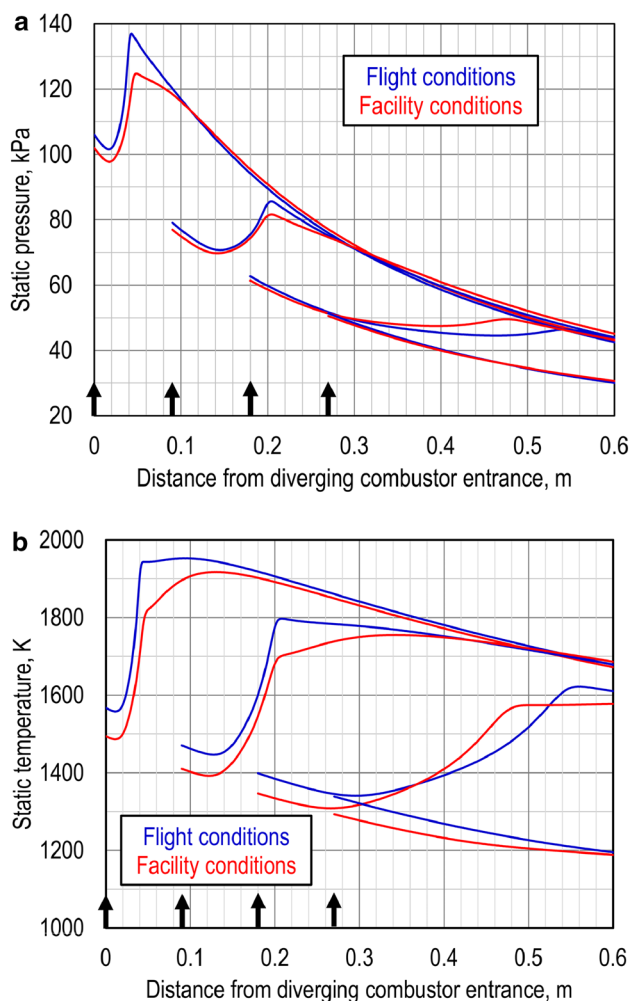


Fig. 4 **a** Static pressure with detailed reaction mechanism. **b** Static temperature with detailed reaction mechanism

conditions. When the second-stage fuel injection location is $x = 0.27$ m, no static pressure increase due to heat release was observed under either. The static temperature and pressure are relatively low at this location, and the reaction is too slow to detect the difference. Based on the above, the present study uses the static pressure distribution at the second-stage fuel injection location of $x = 0.18$ m, where the difference between flight and facility conditions was most noticeable, to reduce and verify the reaction mechanism.

Figure 4b shows the static temperature distributions. At the second-stage fuel injection locations of $x = 0$ and 0.09 m, the static temperature rise is almost the same, but the subsequent increase in static temperature is slower under the facility condition. Here, the effect of static temperature decreases with expanding flow path, and the effect of a static temperature rise by heat release is compete. Under facility conditions that contain H_2O in the airflow, exothermic reactions are suppressed by the H_2O . At the second-stage

fuel injection location of $x = 0.18$ m, the static temperature rises faster in the facility condition. However, heat release continues to compete with the effect of channel expansion downstream from the static pressure peak location. Under the flight condition, the static temperature rises slowly, but the static temperature decreases downstream from the peak location. The static temperature rise is slow until the start of the reaction and then fast until the completion of the subsequent reaction.

To further investigate this reversal behavior of the static temperature (Fig. 4b) for the injection at $x = 0.18$ m, the temperature sensitivity was observed, and the elementary reactions dominant to the static temperature were extracted. Comparing the flight and facility conditions we see that the elementary reaction of (I) $HCO + M = CO + H + M$ with positive temperature sensitivity and two elementary reactions of (II) $C_2H_4 + O = CH_3 + HCO$ and (III) $C_2H_3 + O_2 = HCO + CH_2O$ with negative temperature sensitivity were additionally extracted under flight conditions. Therefore, it is reasonable to assume that the effect of (II) and (III) was greater than the effect of (I), causing the temperature rise under flight conditions to be suppressed compared to under facility conditions. The difference is indirectly caused by the difference between the presence (for the facility) and absence (for flight) of H_2O vitiation. The static temperature distribution also shows that the second-stage fuel injection location of $x = 0.18$ m is suitable for detecting the difference in the results between flight and facility conditions as the difference in peak locations.

By comparing the H_2O distribution (Fig. 5a) and CO_2 distribution (Fig. 5b) obtained in this simulation, the static temperature and pressure increase corresponded to the H_2O production, and the subsequent process after the peak corresponds to the CO_2 production. In other words, the first half of C_2H_4 combustion consists of H_2 combustion, and the second half consists of CO combustion. As shown in Fig. 5a, the difference in H_2O mole fraction between flight and facility conditions indicates the H_2O vitiation for facility conditions.

3.2 Reduction of C_2H_4 /air reaction mechanism by "reaction workbench"

This section discusses the detailed reaction mechanism reduced using CHEMKIN-Pro. USC Mech II was designated the detailed reaction mechanism (the master mechanism). The static pressure distribution under the facility condition for the second-stage fuel injection location at $x = 0.18$ m (see the previous section) was specified as the reproduction target in the reduction process. For the following example, it is assumed that the allowable error for the static pressure distribution is 10%. CHEMKIN-Pro automatically proceeds with the following operations.

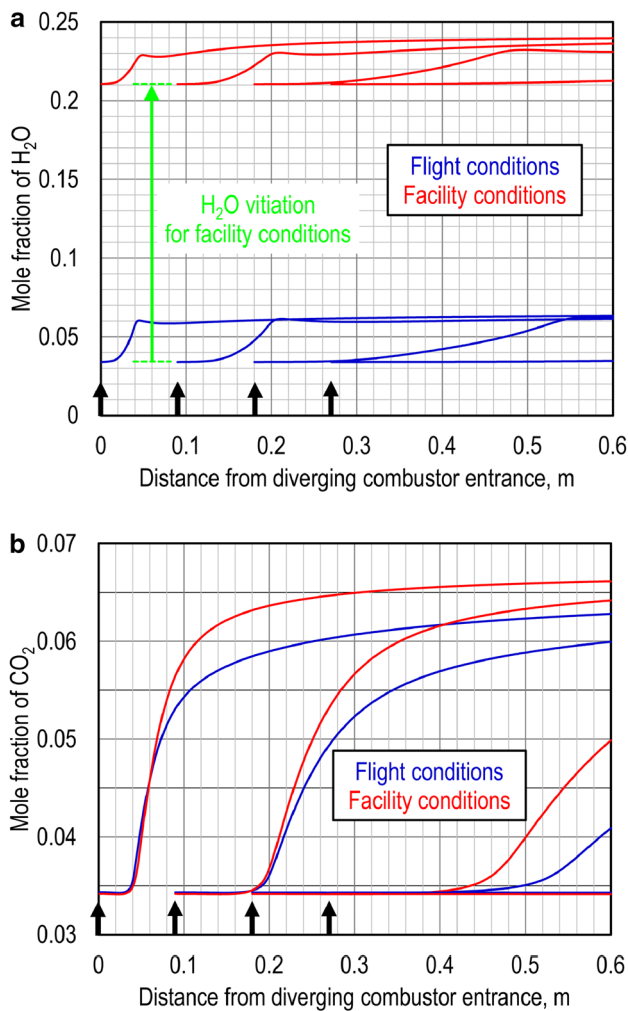


Fig. 5 **a** H_2O mole fraction with detailed reaction mechanism. **b** CO_2 mole fraction with detailed reaction mechanism

- Calculate the static pressure distribution with USC Mech II (the master mechanism).
- Delete low-impact species and related elementary reactions.
- Calculate the static pressure distribution using the reduced reaction mechanism created in (B).
- Calculate the error in (C) by comparing (A) and (C).
- If the result of (D) is 10% or less, perform (B)–(D) again, and otherwise, the reduction is stopped.

Note that some methods are in (B), as shown later. The user specifies one of them in advance.

Figure 6a shows the relationship between the integral pressure thrust increment ratio and the number of species. The integral pressure thrust (F_p) is obtained from the static pressure distribution. The integral pressure thrust increment (ΔF_p) is defined as the difference between F_p with reaction and F_p without reaction, as shown by Eq. 1.

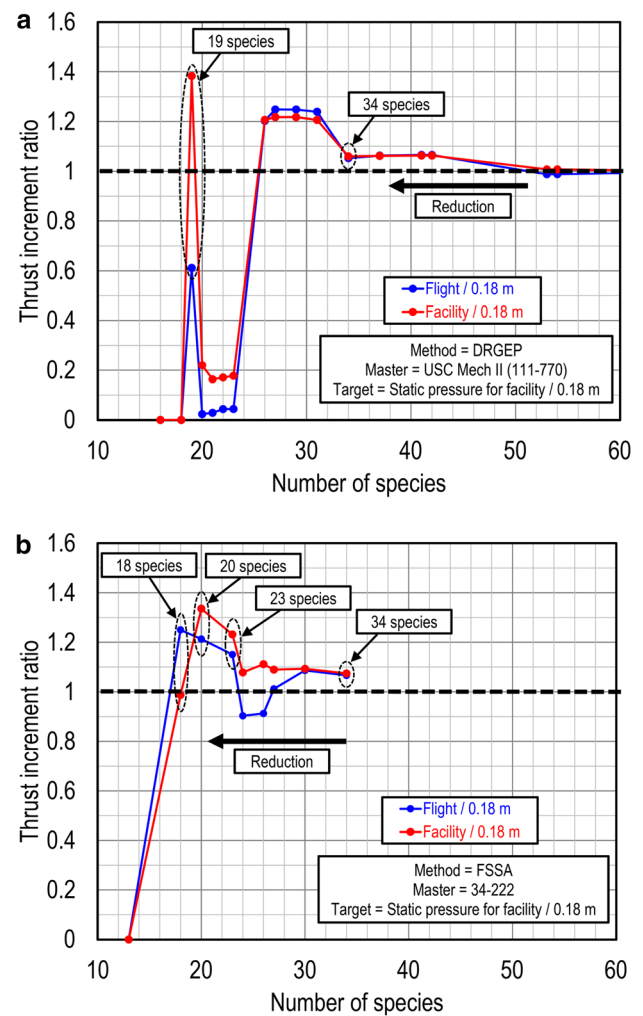


Fig. 6 **a** Reduction of reaction mechanisms by DRGEP method. **b** Reduction of reaction mechanisms by FSSA method

$$\Delta F_p = F_p \Big|_{\text{reac.}} - F_p \Big|_{\text{no-reac.}} \quad (1)$$

The integral pressure thrust increment ratio (r) is defined as the ratio of ΔF_p with reduced reaction mechanism and ΔF_p with a detailed reaction mechanism, as shown by Eq. 2.

$$r = \frac{\Delta F_p \Big|_{\text{reduced}}}{\Delta F_p \Big|_{\text{detailed}}} = \frac{\left(F_p \Big|_{\text{reac.}} - F_p \Big|_{\text{no-reac.}} \right)_{\text{reduced}}}{\left(F_p \Big|_{\text{reac.}} - F_p \Big|_{\text{no-reac.}} \right)_{\text{detailed}}} \quad (2)$$

Therefore, when the static pressure distribution by the reduced reaction mechanism matches that calculated by the detailed reaction mechanism, r equals unity. The larger the deviation from unity, the worse the reproducibility of the static pressure distribution. Here, directed relation graph with error propagation (DRGEP) method [12, 13] was used as the reduction method of (B) above. To observe how the reproducibility

of the static pressure distribution deteriorates due to reduction, an allowable error above 10% is used here.

Reduction of the reaction mechanism proceeds from right to left in the figure. As the number of species is reduced, the reproducibility deteriorates step by step. For example, in Fig. 6a, after maintaining a relatively good reproducibility of up to 34 species, if the number of species falls below 34, a large shift occurs, and a significant deviation occurs at 23 species or fewer. Note that when the number of species falls below 18, the integral pressure thrust increment ratio (r) becomes zero. This case occurs when fuel and airflow leave the diverging combustor before the reaction occurs. However, the reaction occurs in the diverging combustor when using the detailed reaction mechanism. One interesting feature of Fig. 6a is that 19-species mechanisms reduce the deviation compared to 20–23-species mechanisms and improve reproducibility. This 19-species mechanism was included as a candidate for the reduced mechanism. The captions “111–770” in the figure show the set of the numbers of species and elementary reactions. Thus, “111–770” means 111 species and 770 elementary reactions, and this notation will be applied in the rest of this paper. As also shown in the figure, the static pressure distribution for injection at $x=0.18$ m for facility conditions was selected as the reproduction target. The red line in the figure shows the actual reduction process by CHEMKIN-Pro, and the blue line does not. The blue line was plotted by calculating the static pressure distributions for the injection case at $x=0.18$ m under flight conditions using the reduced reaction mechanisms obtained from the red line.

In CHEMKIN-Pro, the full species sensitivity analysis (FSSA) method is also suggested as the final reduction step after DRGEP makes some reductions. The procedure of the FSSA method is as follows [14]:

- Remove each species individually from the smallest skeletal mechanism generated so far and calculate the induced error on target parameters for this species.
- Rank the species using their induced error in ascending order.
- Remove candidate species from the skeletal mechanism in the order prescribed in step (b) and calculate the cumulative induced error on the target parameters after each species is removed.
- Stop the process when the cumulative induced error exceeds the specified tolerance level.

For example, Liu et al. [15] applied some reduction methods, including FSSA, to obtain the reduced reaction mechanism for a laminar premixed flame of ethanol/acetone mixtures. In the present study, a 34-species mechanism was selected as the master mechanism for the FSSA method because it was the smallest mechanism in which the deviation in the integral pressure thrust increment (r) was within 10% by the DRGEP method. Figure 6b shows the relationship between the number of species and r , obtained by the FSSA method. To observe how the reproducibility of the static pressure distribution deteriorates due to reduction, a value larger than 10% was specified as an allowable error. The 34-, 23-, 20-, and 18-species mechanisms were candidates for the reduced mechanisms. Note that the reaction does not occur in the diverging combustor when the number of species is 13 or fewer.

As a result, 34-, 23-, 20-, and 18-species mechanisms were selected as primary candidates, and the 19-species mechanism was selected as a secondary one. These candidates are compared to the 111-species mechanism (USC Mech II) in the present study. Table 2 shows that the deviation in the integral pressure thrust increment ratio (r) of these five reduced mechanisms was around 40% at most in the case of the 19-species mechanism under flight and facility conditions. The set of species for these reduced mechanisms is shown in Table 3. The table shows that the 19–71 model is categorized into a different group from other reduced mechanisms.

Previously, Varatharajan et al. obtained a 34–148 model for C_2H_4 oxidation [16] and reduced this model to 21–38 [17]. We compared Varatharajan’s 34–148 model to the 34–222 one in this study; C_2H_4O , C_2H , C_3H_7 , C_3H_6 , and C_3H_3 are included only in the 34–148 model, and CH_3OH , H_2CC , and C_2O are included only in 34–222 model. In the same way, when comparing Varatharajan’s 21–38 model to the 20–96 model of this study, C_2H_5 , H_2O_2 , CH_2CO , and C_2H_4O are included only in the 21–38 model, and CH_2^* , CH_3O , and CH_2 are included only in 20–96 model. Of course, these differences arise because the simulation target in the present study is a specific scramjet combustor with specific conditions. This suggests one should use a custom-made reaction mechanism dedicated to that simulation target to perform a particular reaction simulation.

For the 34–222, 23–121, 20–96, 18–63, and 19–71 models, the comparison results with the detailed reaction mechanism (111–770 model) focusing on the static pressure distribution for injection at $x=0.18$ m are shown in Fig. 7a (flight conditions) and Fig. 7b (facility conditions), which are also the basis of Table 2. The static temperature distributions are also shown in Fig. 8a (flight conditions) and Fig. 8b (facility

Table 2 Integral pressure thrust increment ratio (r) for reduced reaction mechanisms

| Conditions | 111–770 | 34–222 | 23–121 | 20–96 | 18–63 | 19–71 |
|------------|----------|--------|--------|-------|-------|-------|
| Flight | 1 (ref.) | 1.066 | 1.151 | 1.213 | 1.250 | 0.611 |
| Facility | 1 (ref.) | 1.074 | 1.232 | 1.336 | 0.987 | 1.382 |

Table 3 Chemical species included in reduced reaction mechanisms

| No. | Species | 34–222 | 23–121 | 20–96 | 18–63 | 19–71 |
|-----|--------------------------------|--------|--------|-------|-------|-------|
| 1 | N ₂ | ● | ● | ● | ● | ● |
| 2 | H | ● | ● | ● | ● | ● |
| 3 | O | ● | ● | ● | ● | ● |
| 4 | OH | ● | ● | ● | ● | ● |
| 5 | HO ₂ | ● | ● | ● | ● | ● |
| 6 | H ₂ | ● | ● | ● | ● | ● |
| 7 | H ₂ O | ● | ● | ● | ● | ● |
| 8 | O ₂ | ● | ● | ● | ● | ● |
| 9 | CH ₂ * | ● | ● | ● | ● | ● |
| 10 | CH ₃ | ● | ● | ● | ● | ● |
| 11 | HCO | ● | ● | ● | ● | ● |
| 12 | CO | ● | ● | ● | ● | ● |
| 13 | CO ₂ | ● | ● | ● | ● | ● |
| 14 | C ₂ H ₃ | ● | ● | ● | ● | ● |
| 15 | C ₂ H ₄ | ● | ● | ● | ● | ● |
| 16 | CH ₂ CHO | ● | ● | ● | ● | ● |
| 17 | CH ₃ O | ● | ● | ● | ● | – |
| 18 | C ₂ H ₂ | ● | ● | ● | ● | – |
| 19 | CH ₂ | ● | ● | ● | – | ● |
| 20 | CH ₂ O | ● | ● | ● | – | – |
| 21 | CH ₄ | ● | ● | – | – | – |
| 22 | CH ₃ OH | ● | ● | – | – | – |
| 23 | HCCO | ● | ● | – | – | – |
| 24 | H ₂ CC | ● | – | – | – | ● |
| 25 | C ₂ H ₅ | ● | – | – | – | ● |
| 26 | CH ₂ OH | ● | – | – | – | – |
| 27 | C ₂ O | ● | – | – | – | – |
| 28 | H ₂ O ₂ | ● | – | – | – | – |
| 29 | CH | ● | – | – | – | – |
| 30 | C ₂ H ₆ | ● | – | – | – | – |
| 31 | CH ₂ CO | ● | – | – | – | – |
| 32 | pC ₃ H ₄ | ● | – | – | – | – |
| 33 | aC ₃ H ₄ | ● | – | – | – | – |
| 34 | aC ₃ H ₅ | ● | – | – | – | – |

conditions). The 34–222 and 23–121 models reproduce the results of 111–770 model well. These two models commonly show that a reduction of reaction mechanism results in reaction promotion. The 20–96 model results have a similar distribution to those for the 23–121 model, but the distribution is sluggish. The result for the 18–63 model trends differently from the mechanisms mentioned above, and the heat release is faster than for the 111–770 model, as seen in Figs. 7 and 8. The peak pressure is higher for both conditions (Fig. 7a, b), but the peak temperature is lower for both (Fig. 8a, b). The 19–71 model results show different (or opposite) features under flight and facility conditions. Compared to the 111–770 model results, the heat release is slower under flight conditions (Figs. 7a and 8a) but faster under facility conditions (Figs. 7b, 8b). From 1D analysis, the 34–222 and 23–121 models are “excellent,”

the 20–96 model is “fair,” and the 18–63 and 19–71 models are “poor” in terms of the reproducibility of 111–770 model results.

4 Validation 1: 0D ignition delay simulation by “perfectly stirred reactor” model

This section discusses the ignition delay evaluated by a perfectly stirred reactor (PSR) model that can be simulated with CHEMKIN-Pro as another index for selecting a reduced reaction mechanism. The parameters for simulation, namely, pressure and initial composition, are based on flight and facility conditions for injection at $x=0.18$ m in the 1D simulation. The initial temperature is set to 1200–1800 K. These

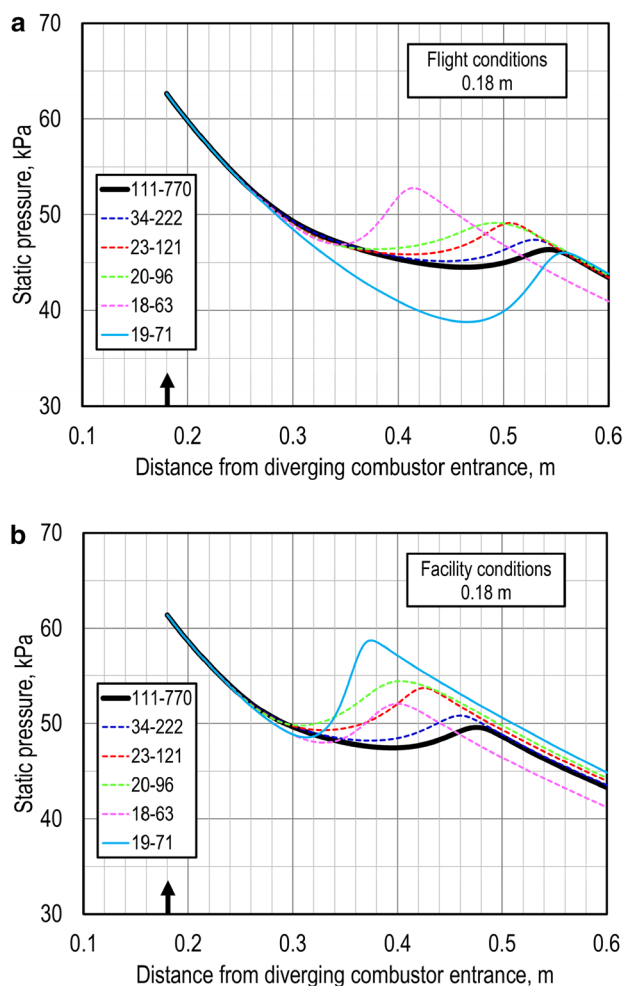


Fig. 7 **a** Master model vs. reduced models for static pressure (flight conditions). **b** Master model vs. reduced models for static pressure (facility conditions)

parameters correspond to those for injection at $x = 0.18$ m, used for 1D PFR simulation, as shown in Table 1a, b. Ignition is defined as the moment at which dT/dt is maximum (the temperature inflection point), and the required time from the start of calculation to ignition is defined as the ignition delay.

Figure 9a shows the relationship between the initial temperature and the ignition delay. The candidates for the reduced reaction mechanism include all sets of the 34–222, 23–121, 20–96, 18–63, and 19–71 models examined in the previous section. The upper half (left axis) shows the results under flight conditions; the lower half (right axis) shows the results under facility conditions. The ignition delay was normalized by the value calculated with the detailed reaction mechanism (111–770 model), which is a reproduction target. Therefore, the closer the value is to unity, the better the reproducibility of the ignition delay in the detailed reaction mechanism. Interestingly, the reductions result in ignition

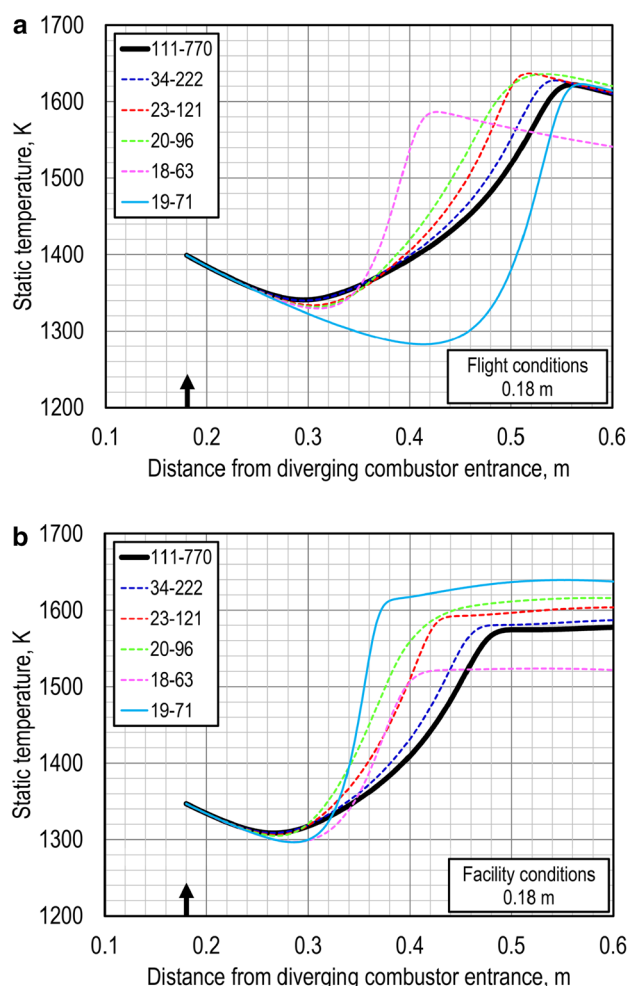


Fig. 8 **a** Master model vs. reduced models for static temperature (flight conditions). **b** Master model vs. reduced models for static temperature (facility conditions)

promotion below 1500 K and ignition suppression above 1500 K, except for the 19–71 model. Ignition delays for the 34–222 and 23–121 models show better reproducibility than for the 20–96, 18–63, and 19–71 models.

Figure 9b shows the ratio of the ignition delay under facility conditions to that under flight conditions. This study aims to reproduce the difference between these two sets of conditions. Thus, when the ignition delay is the focus, the ratio between them is also important in addition to the ignition delay itself. The feature common to all reaction mechanisms is that the ignition delay under facility conditions is shorter than that under flight conditions (i.e., the ratio is less than unity). This corresponds to the static pressure peak appearing further upstream in the facility condition in Fig. 7a, b (except for the 18–63 model), and the result of the 1D simulation, the calculated static pressure distribution, and the 0D simulation used to calculate the ignition delay are consistent. These facts suggest that H_2O vitiation promotes

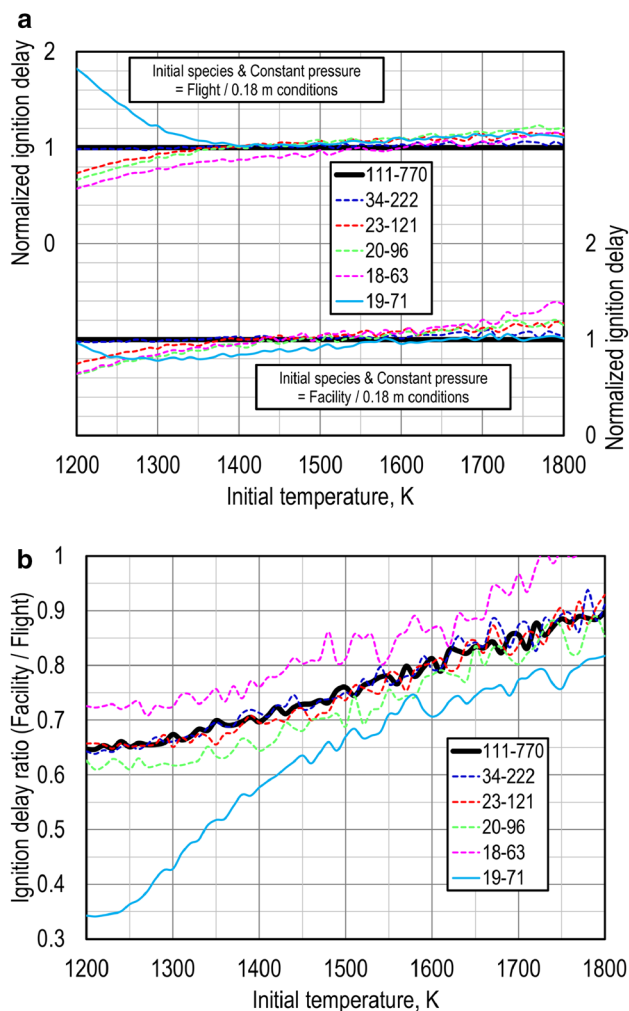


Fig. 9 **a** Normalized ignition delay (flight and facility conditions). **b** Ignition delay ratio (facility/flight)

C_2H_4 combustion even though it suppresses H_2 combustion [2]. However, the effect of H_2O vitiation on C_2H_4 combustion requires careful consideration, as will be discussed later for 2D and 3D simulations. If one should select one model as a reduced reaction mechanism that reproduces the ignition delay ratio of the detailed reaction mechanism well, the 34–222 and 23–121 models are candidates, and the same conclusion as in the previous 1D simulation is drawn. The 34–222 and 23–121 models are “excellent,” the 20–96 model is “fair,” and the 18–63 and 19–71 models are “poor” in terms of their reproducibility of the result of the 111–770 model.

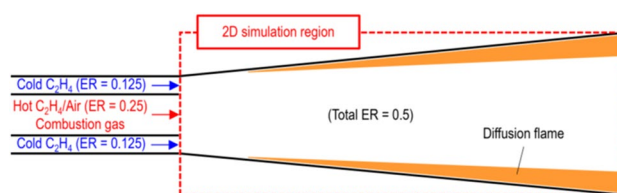


Fig. 10 Combustor configuration for 2D simulation

5 Validation 2: 2D reacting flow simulation

Using the reduced mechanism candidates obtained so far, this section describes a 2D reacting flow simulation done using the commercial software, CRUNCH CFD [18]. A 2D simulation is closer to the actual combustion field than 0D and 1D simulations because it includes diffusion and mixing processes. Since it is possible to use a detailed reaction mechanism for a 2D reacting flow simulation, the effectiveness of each candidate can be verified directly. In addition to the detailed mechanism (111–770 model), the reduced mechanisms of the 34–222, 23–121, 20–96, 18–63, and 19–71 models were applied in this section.

Figure 10 shows the combustor configuration for 2D simulation. The simulation target was the diverging combustor with a length of 0.6 m and a diverging angle of 2° on each side (4° total), similar to the 1D reacting flow simulation. C_2H_4 /Air equilibrium combustion gas, including the first-stage fuel (equivalence ratio of 0.25), flows into the diverging combustor, diffusing and mixing with the second-stage fuel (equivalence ratio of 0.25), then the combustion reaction starts. Note that the primary objective of this 2D simulation is not to reproduce the actual flow field but to compare the features of reaction between the detailed and reduced reaction mechanisms with a simple flow field as much as possible. Therefore, parallel fuel injection to the mainstream from the wall side slit was adopted, whereas the actual second-stage fuel injection was perpendicular to the mainstream. Since the parallel fuel injection can cause combustion to occur far downstream, $x=0$ m was selected as the second-stage fuel injection location for the longest residence time in the combustor. To suppress wave generation, the static pressure at the cold fuel injection port was equalized with the static pressure of the hot main flow by adjusting the cross-sectional area of the cold fuel flow path. The input parameters at the diverging combustor entrance were obtained using the same process as in the 1D simulation and are shown in Table 4a, b for flight and facility conditions, respectively. The parameters in Table 4a, b are the same as for the 1D simulation. However, the parameters are different from those in Table 1a, b due to the conversion from 1D simulation conditions to 2D simulation conditions.

Table 4 Input parameters for 2D simulation for (a) flight conditions, (b) facility conditions

| | Hot main flow | Cold fuel flow |
|-------------------------------|---------------|----------------|
| (a) Flight conditions | | |
| Static pressure, kPa | 104.3 | 104.7 |
| Static temperature, K | 1601.8 | 287.8 |
| Mach number | 1.641 | 1.02 |
| Velocity, m/s | 1268.1 | 332.5 |
| Density, kg/m ³ | 0.2260 | 1.228 |
| Mole fraction | | |
| C ₂ H ₄ | – | 1.000E+00 |
| CO ₂ | 3.495E–02 | – |
| H ₂ O | 3.463E–02 | – |
| N ₂ | 7.752E–01 | – |
| O ₂ | 1.551E–01 | – |
| OH | 8.480E–05 | – |
| (b) Facility conditions | | |
| Static pressure, kPa | 99.7 | 99.8 |
| Static temperature, K | 1521.9 | 287.8 |
| Mach number | 1.696 | 1.02 |
| Velocity, m/s | 1309.6 | 332.5 |
| Density, kg/m ³ | 0.2131 | 1.170 |
| Mole fraction | | |
| C ₂ H ₄ | – | 1.000E+00 |
| CO ₂ | 3.479E–02 | – |
| H ₂ O | 2.143E–01 | – |
| N ₂ | 5.959E–01 | – |
| O ₂ | 1.549E–01 | – |
| OH | 1.113E–04 | – |

Figure 11a, b shows the contours of static pressure and static temperature, respectively. Each figure includes the results under flight conditions (left side) and facility conditions (right side). Regarding the pressure (Fig. 11a), since the main flow is a parallel flow at the diverging combustor entrance (i.e., the exit of the constant cross-sectional area combustor), an expansion wave from the diverging combustor entrance is inevitable in static pressure distributions. The wave structure visible in the figure starts with this expansion wave. Regarding the temperature (Fig. 11b), on the other hand, since the equilibrium combustion gas from the constant cross-sectional area combustor flows into the diverging combustor section, the temperature of the entire analysis field is high (static temperature of about 1600 K). The second-stage fuel is injected parallel to the mainstream at the diverging combustor entrance, that is, at an angle of 2° with respect to the wall of the diverging combustor. The reaction region gradually develops near the wall surface in the static temperature distributions. Looking at the distributions in Fig. 11a and 11b, there is almost no difference between the results of the 34–222, 23–121, 20–96, and 18–63 models and

the 111–770 model. Only the 19–71 model shows a different feature from other models. More specifically, the origin of the flame is slightly downstream, but the flame is slightly thicker. This delayed but intensive flame generation causes an intense shock wave from the origin of the flame, and an elevated temperature and pressure region appears at the intersection of the two shock waves.

The static pressure distribution in x direction on the wall surface is undulating due to the incidence of waves, making it difficult to compare the results among these reaction mechanisms. Therefore, the distributions of the mass flow weighted average values of static pressure for these six reaction mechanisms (the 111–770, 34–222, 23–121, 20–96, 18–63, and 19–71 models) are shown in Fig. 12a (flight conditions) and Fig. 12b (facility conditions). The features observed in Fig. 12a, b are the same. As the reduction progresses, the reaction accelerates, and the static pressure peak location shifts upstream. Further, although the difference is slight, the degree of reaction promotion is greater in Fig. 12b (facility conditions) than in Fig. 12a (flight conditions). These static pressure features are consistent with the 1D reacting flow simulation results shown in Fig. 7a, b.

The distributions of the mass flow weighted average values of static temperature are shown in Fig. 13a (flight conditions) and Fig. 13b (facility conditions). With the same features that the reaction accelerated, the static temperature peak location shifts upstream as the reduction progresses, and the degree of reaction promotion is greater in Fig. 13b (facility conditions), as shown. The static temperature distribution for the 18–63 model shows a different trend from the other four mechanisms (the 111–770, 34–222, 23–121, and 20–96 models), namely, a lower static temperature. These static temperature features are consistent with the 1D reacting flow simulation results shown in Fig. 8a, b. In addition, the 19–71 model clearly shows different static pressure and temperature distributions from the other five mechanisms (the 111–770, 34–222, 23–121, 20–96, and 18–63 models). The distributions of the 19–71 model have multiple peaks, indicating that the peaks are not due to reactions but are due to local wave interference, as can be seen in Fig. 11a. From 2D analysis, it seems that the 34–222 model is “excellent,” 23–121 and 20–96 models are “fair,” and 18–63 and 19–71 models are “poor” in terms of the reproducibility of the results of 111–770 model.

One more important feature in Figs. 12 and 13 is that the peak locations of the temperature and pressure for the 111–770 model were further downstream for facility conditions, suggesting that H₂O vitiation suppresses the C₂H₄ combustion, which is inconsistent with the results of the 0D and 1D simulations. The effect of H₂O vitiation on C₂H₄ combustion requires careful consideration.

Comparing the diffusion flame structures of the six reaction mechanisms (the 111–770, 34–222, 23–121,

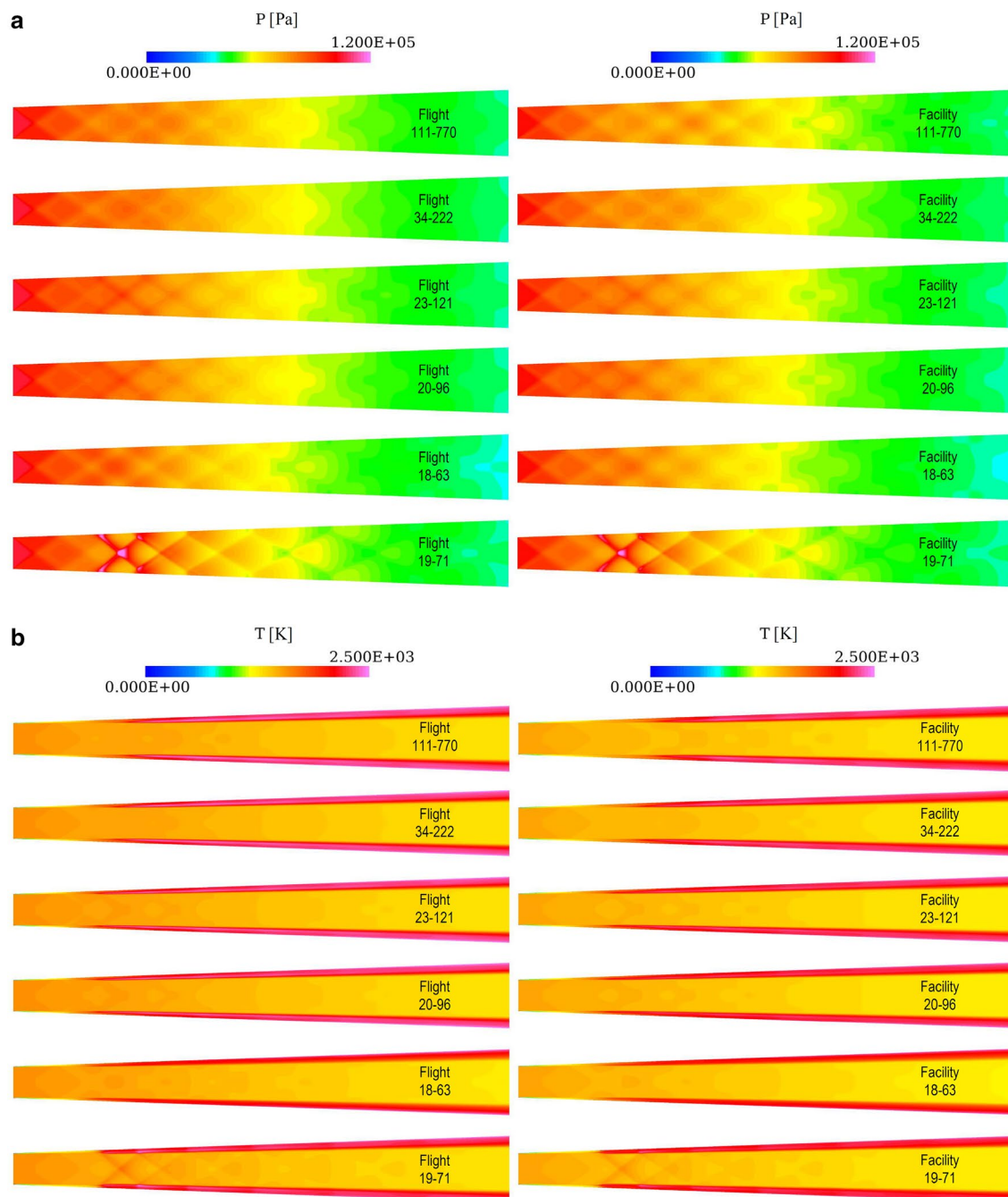


Fig. 11 **a** 2D contour of static pressure for flight (left) and facility (right) conditions. **b** 2D contour of static temperature for flight (left) and facility (right) conditions

20–96, 18–63, and 19–71 models), the static temperature and mole fraction distributions in the y direction are shown in Fig. 14a (flight conditions) and Fig. 14b (facility conditions). All figures show the distributions at $x = 0.2$ m. The center line of the flow path is at $y = 0$ m, and the solid line at $y = 0.026$ m represents the wall in the figure. As shown in Fig. 11b, the diffusion flame (the reaction zone) appears near the fuel-side

(wall-side) distributions, it is interesting that H_2 and CO replace C_2H_4 . In addition, the diffusion flame (the reaction zone) is slightly thicker for the 19–71 model, as can be observed in Fig. 11b. For each condition, the 34–222, 23–121, and 20–96 models have distributions similar to 111–770 model, but the 18–63 and 19–71 models trend differently from other four mechanisms. Notably, the peak static temperature within the reaction zone is lower. This

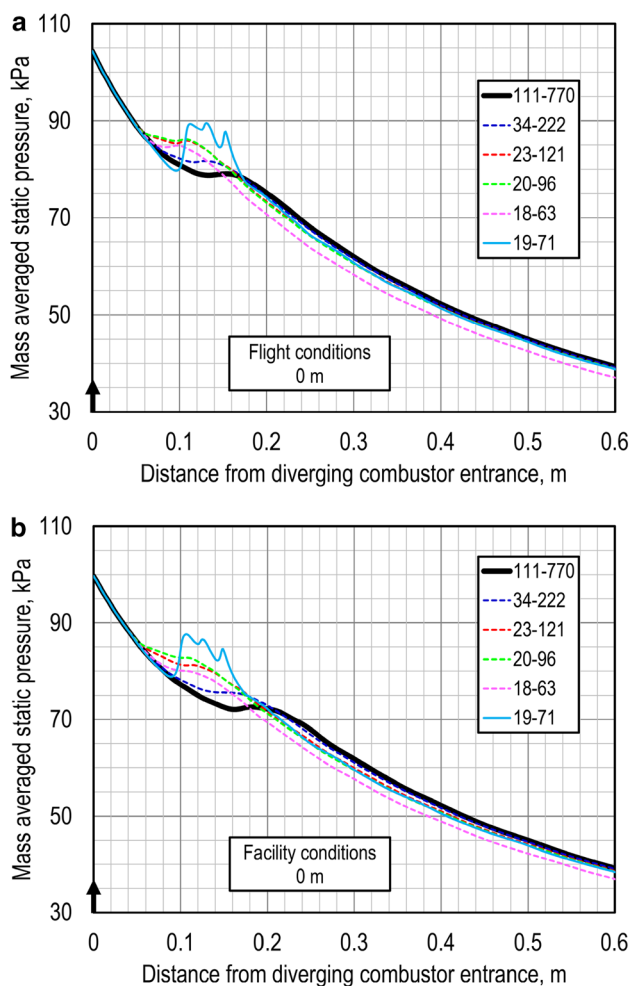


Fig. 12 **a** Master model vs. reduced models for mass averaged static pressure (flight conditions). **b** Master model vs. reduced models for mass averaged static pressure (facility conditions)

feature corresponds to the 1D and 2D simulations' results. Since the reaction rate is an exponential function of the temperature (i.e., the Arrhenius equation), the reaction is highly sensitive to temperature. Therefore, a reduced reaction mechanism must precisely reproduce a temperature distribution. Thus, the 18–63 and 19–71 models should not be selected as reduced mechanisms.

6 Validation 3: 3D reacting flow simulation

In the final validation step, a 3D reacting flow simulation was performed. Since the 3D simulation requires a long computational time, the computational domain was limited to the isolator and combustor (the inlet was not included). Figure 15a shows the flow-path configuration for the 3D simulation. The flow path consists of a constant cross-sectional area isolator with a length of 0.2 m (x direction) and

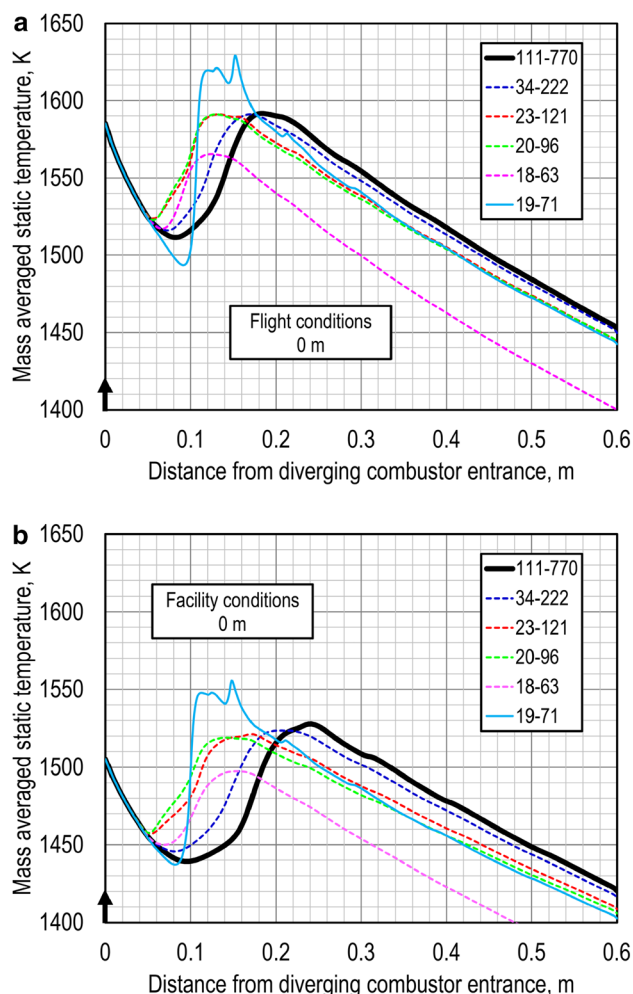


Fig. 13 **a** Master model vs. reduced models for mass averaged static temperature (flight conditions). **b** Master model vs. reduced models for mass averaged static temperature (facility conditions)

a diverging combustor, which has two cavities and the first- and second-stage fuel injectors, with a length of 0.6 m and a diverging angle of 1.3° on each side (2.6° total). Note that the constant cross-sectional area combustor, considered in 1D and 2D simulations, was not applied in 3D simulation due to optimization of the combustor design. The fuel injection angles were 15° and 90° for the first- and second-stage injectors, respectively. The size of the isolator entrance was 50.8 mm (2 in.) in width (y direction) and 38.1 mm (1.5 in.) in height (z direction). More detail on the combustor configuration is given in Ref. [19].

3D-RANS simulations were conducted using a JAXA in-house solver, LS-FLOW, a finite-volume compressible flow solver for arbitrary unstructured grids, originally developed for aerodynamic simulation of an external flow around flying vehicles [20]. The solver is an extended version of LS-FLOW, which can accommodate arbitrary chemical species and reaction mechanisms. ERENA [21] is implemented in

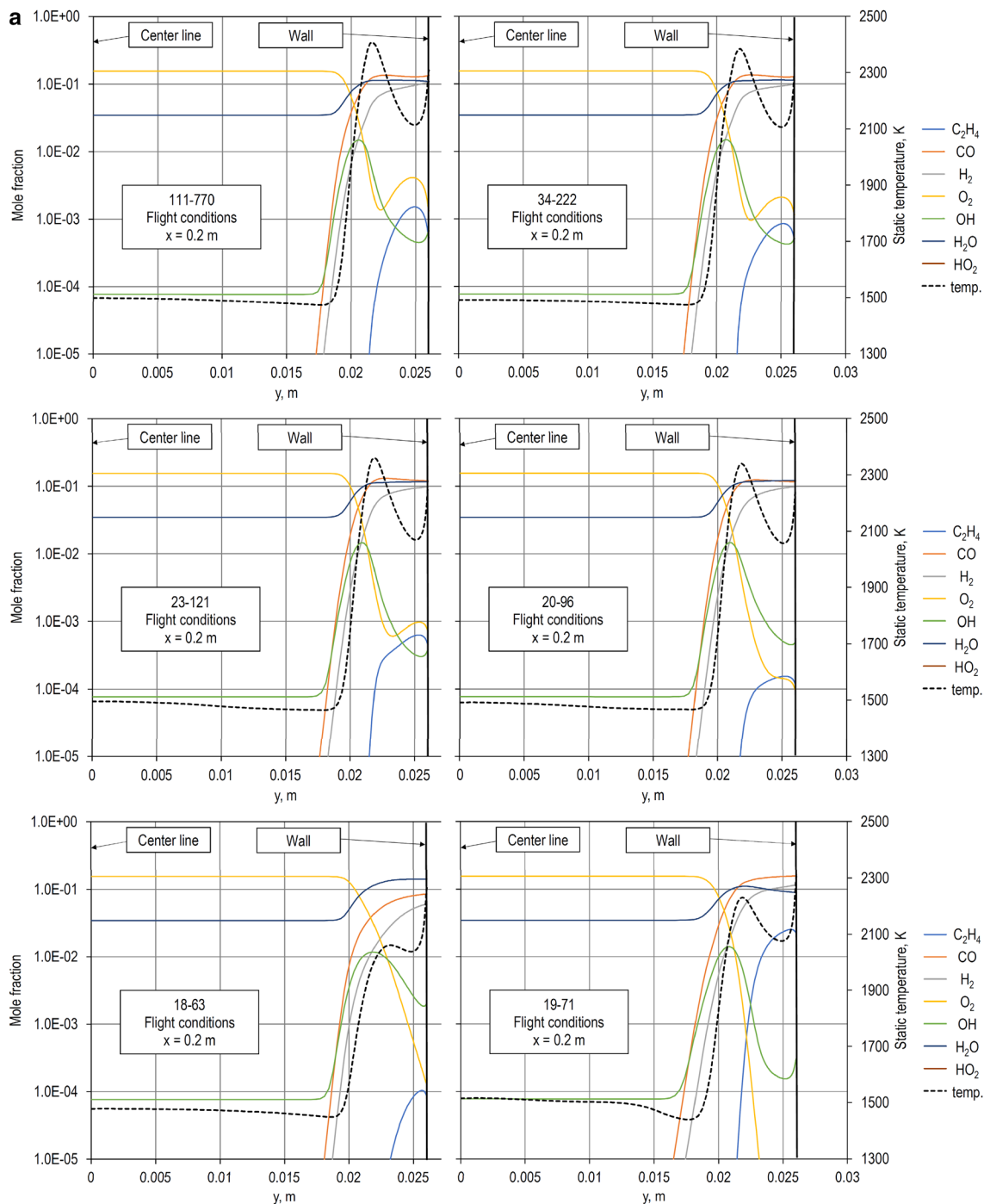


Fig. 14 **a** Diffusion flame structure in diverging combustor at $x=0.2$ m (flight conditions). **b** Diffusion flame structure in diverging combustor at $x=0.2$ m (facility conditions)

LS-FLOW for time integration of the chemical source term, allowing the solver to efficiently compute reaction mechanisms involving many chemical species, such as the combustion process of hydrocarbon fuels. In each time step, the time integration of the chemical source term and that of the other terms of the governing equations are executed separately

and alternately using ERENA and LU-SGS implicit methods [22], respectively. The convection and viscous terms of the governing equations were discretized by the SLAU2 scheme [23] with second-order MUSCL interpolation [24] and second-order centered scheme, respectively. The whole flow field in the combustor was assumed to be fully turbulent, and

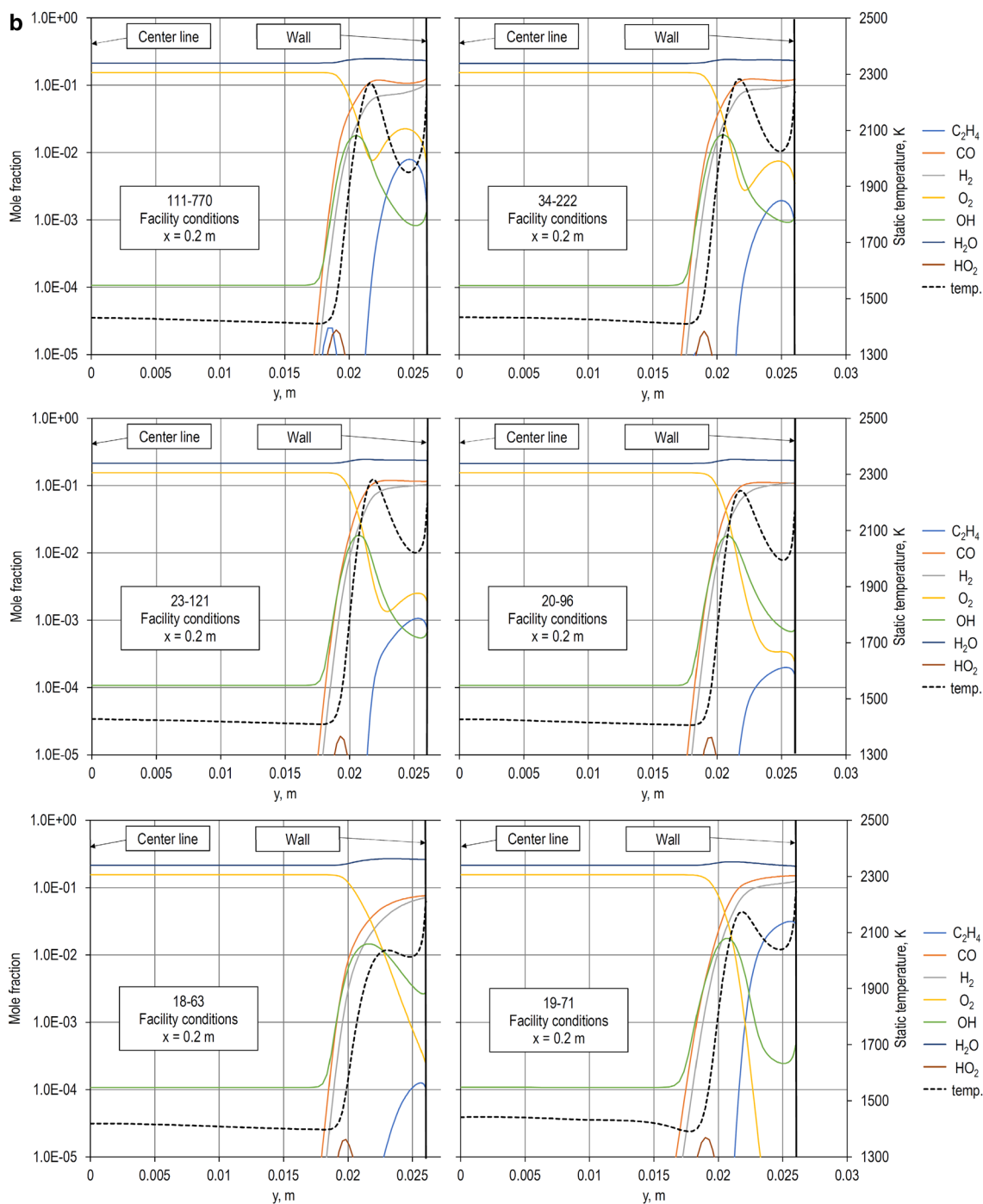


Fig. 14 (continued)

Menter’s SST-V model [25] was used to evaluate the turbulence effect. However, modeling for turbulence-chemistry interaction was not applied in the present simulation. It is known that the turbulent Schmidt number strongly affects the turbulent mixing process. According to previous works [26, 27], the turbulent Schmidt number of 0.3 gave better agreement between simulation and experiment than a large

value, such as 0.9, for a combustor flow in supersonic combustion mode. Therefore, the turbulent Schmidt number was set to 0.3 in the simulation. The turbulent Prandtl number was set to 0.89. The unstructured grid used in the present simulation is shown in Fig. 15b (a quarter of the volume shown in Fig. 15a). There were 1.4 million nodes and 3.4 million elements. The cell thickness in the vicinity of the

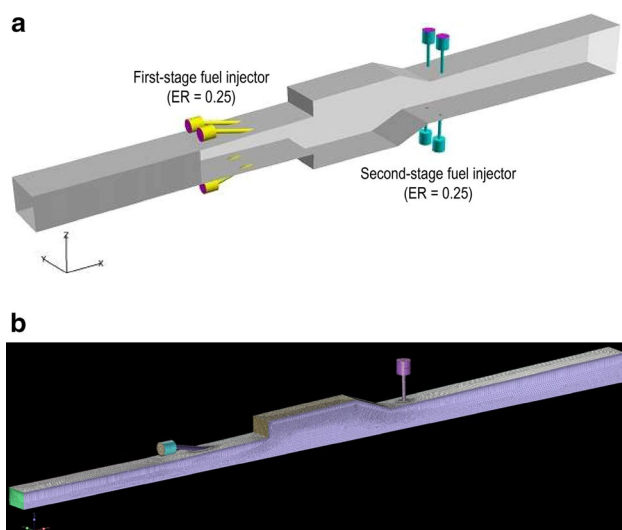


Fig. 15 **a** Combustor configuration for 3D simulation. **b** Unstructured grid configuration for 3D simulation

combustor wall was 10 μm . The simulation was conducted on the JAXA Supercomputer System 2 (JSS2).

Figure 16 shows the input parameter calculation process for 3D simulation. First, the flight Mach number was set to 6.1, and the ambient air conditions, namely the static pressure and temperature, were set to 2.4 kPa and 222 K. The corresponding dynamic pressure was 62.5 kPa. Regarding flight conditions, the inflow condition was obtained from the flight Mach number and ambient air parameters mentioned above by a “non-reacting” 3D simulation around the forebody of the flight test model, which included the inlet and the internal flow path of the isolator [(1) and (2) in Fig. 16].

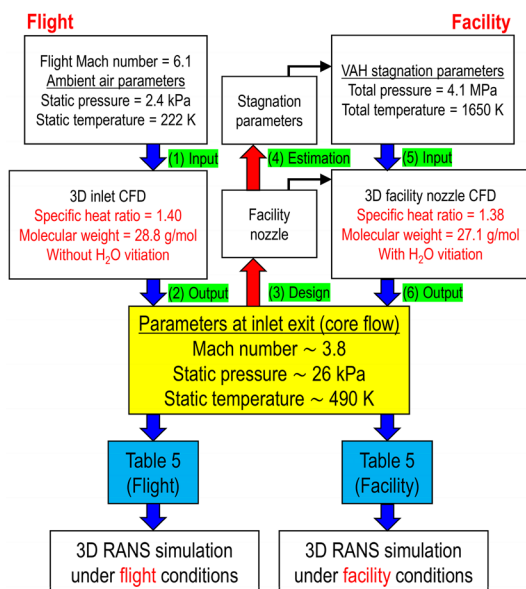


Fig. 16 Input parameter calculation process for 3D simulation

The parameters at the inlet exit, which are shown in the yellow box in Fig. 16, are common to the flight and facility conditions in 3D simulation. Note that these parameters are the mass flow weighted average values of the core flow, not the entire cross-section. Regarding facility conditions, a direct-connect setup consisting of a facility nozzle and isolator (these are directly connected) was assumed. Then, a facility nozzle was designed [(3) in Fig. 16] to obtain the parameters at the inlet exit (shown in the yellow box in Fig. 16), and the required stagnation parameters in the vitiation air heater (VAH) were estimated [(4) in Fig. 16]. In these procedures of nozzle design and stagnation parameter estimation, H_2O vitiation (15% in mass fraction) was considered. Using the estimated VAH stagnation parameters and designed facility nozzle, a 3D “reacting” nozzle flow simulation was done to obtain the parameters at the inlet exit for facility conditions [(5) and (6) in Fig. 16]. The parameters at the inlet exit for the 3D simulation are also the mass flow weighted average values of the core flow, as shown in Table 5. The difference in parameters between flight and facility conditions shows the errors from the procedures of nozzle design and stagnation parameter estimation. Since this 3D simulation has been performed independently from earlier 1D simulations, the methodologies for setting the common parameters between flight and facility conditions were different, as shown in Figs. 3 and 16. However, both methodologies are valid for the investigations of this study.

The fuel is C_2H_4 , and the equivalence ratio for the first- and second-stage injections is 0.25 (0.5 in total). Since the 111–770 model cannot be applied to the 3D reacting flow simulation because of the mechanism size, the 34–222 model (evaluated as “excellent” in 0D, 1D, and 2D analyses) was applied as the master mechanism (the reproduction target). Therefore, the 34–222, 23–121, 20–96, 18–63, and 19–71 models were applied in this section.

Figure 17 shows the 3D distributions of the static temperature under flight conditions (left side) and facility conditions (right side). These figures show that the relatively low-temperature core flow is maintained to the combustor exit. The first-stage fuel was burned in the entire region of the cavity, and the second-stage fuel was burned in the vicinity

Table 5 Input parameters for 3D simulation for flight and facility conditions

| | Flight conditions | Facility conditions |
|---------------------------------------|-------------------|---------------------|
| Static pressure, kPa | 25.8 | 28.9 |
| Static temperature, K | 485 | 503 |
| Mach number | 3.79 | 3.78 |
| Mass fraction of H_2O | – | 0.15 |
| Mass flow rate, g/s | 599.0 | 632.4 |

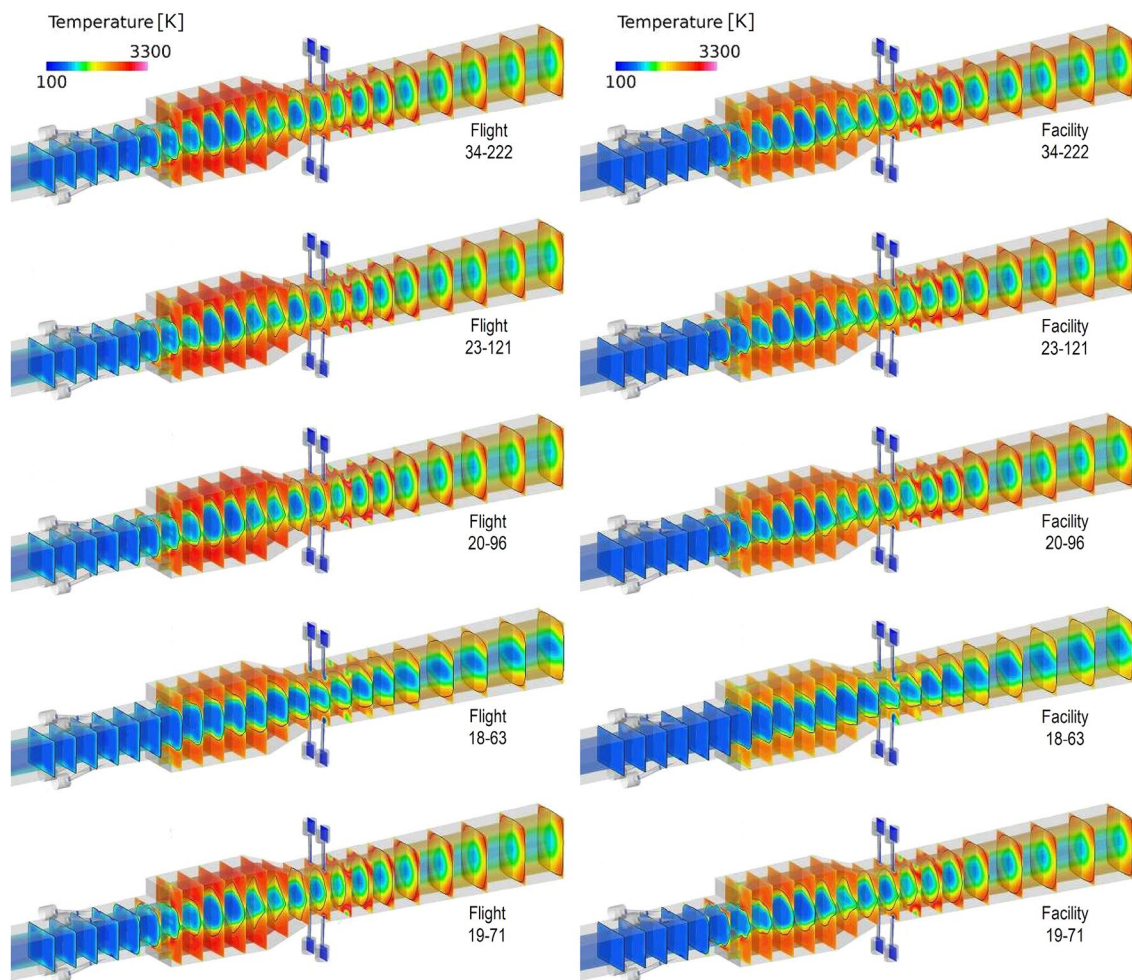


Fig. 17 3D contour of static temperature for flight (left) and facility (right) conditions

of the combustor wall, especially in the corner region. The difference in temperature distributions between flight and facility conditions looks small, but a slightly higher temperature was observed in the cavity under flight conditions rather than facility conditions. Regarding the reaction mechanisms, the 23–121, 20–96, and 19–71 models reproduce the flow structure of the master mechanism (the 34–222 model). Only the 18–63 model shows a weaker heat release than the other four mechanisms (the 34–222, 23–121, 20–96, and 19–71 models).

To better understand the flow structure, the static temperature contours in the XZ plane at $y = 0$ mm (on the spanwise center line) and $y = 12.7$ mm (on the first- and second-stage fuel injector line) are shown in Fig. 18a, b, respectively. The solid black line shows the sonic line. These figures show that the core flow is supersonic and has a continuous pattern of compression and expansion. The core flow in Fig. 18b ($y = 12.7$ mm) is thinner than that in Fig. 18a ($y = 0$ mm) because the effect of compression by combustion is stronger along the fuel injector line ($y = 12.7$ mm). This means that

the thickness of the core flow is distributed spanwise. In addition, the combustion in the cavity is weaker around the upstream step (or backward-facing step) in Fig. 18a, showing that the heat release in the cavity also is distributed spanwise, especially around the upstream step. When comparing the temperature distributions between the flight and facility conditions, the thermal boundary layer in the isolator can be seen more clearly under flight conditions. However, almost no difference can be observed after the fuel combustion starts. Regarding the reaction mechanism, the 23–121, 20–96, and 19–71 models reproduced the flow structure of the master mechanism (34–222 model). As shown in Fig. 17, only the 18–63 model showed a weaker heat release in the cavity than the other four mechanisms (the 34–222, 23–121, 20–96, and 19–71 models), and thus, the pattern of compression and expansion in the core flow was also weaker. As a result, the starting location of the temperature rise was an upstream cavity step only for the 18–63 model, while the other four mechanisms (the 34–222, 23–121, 20–96, and

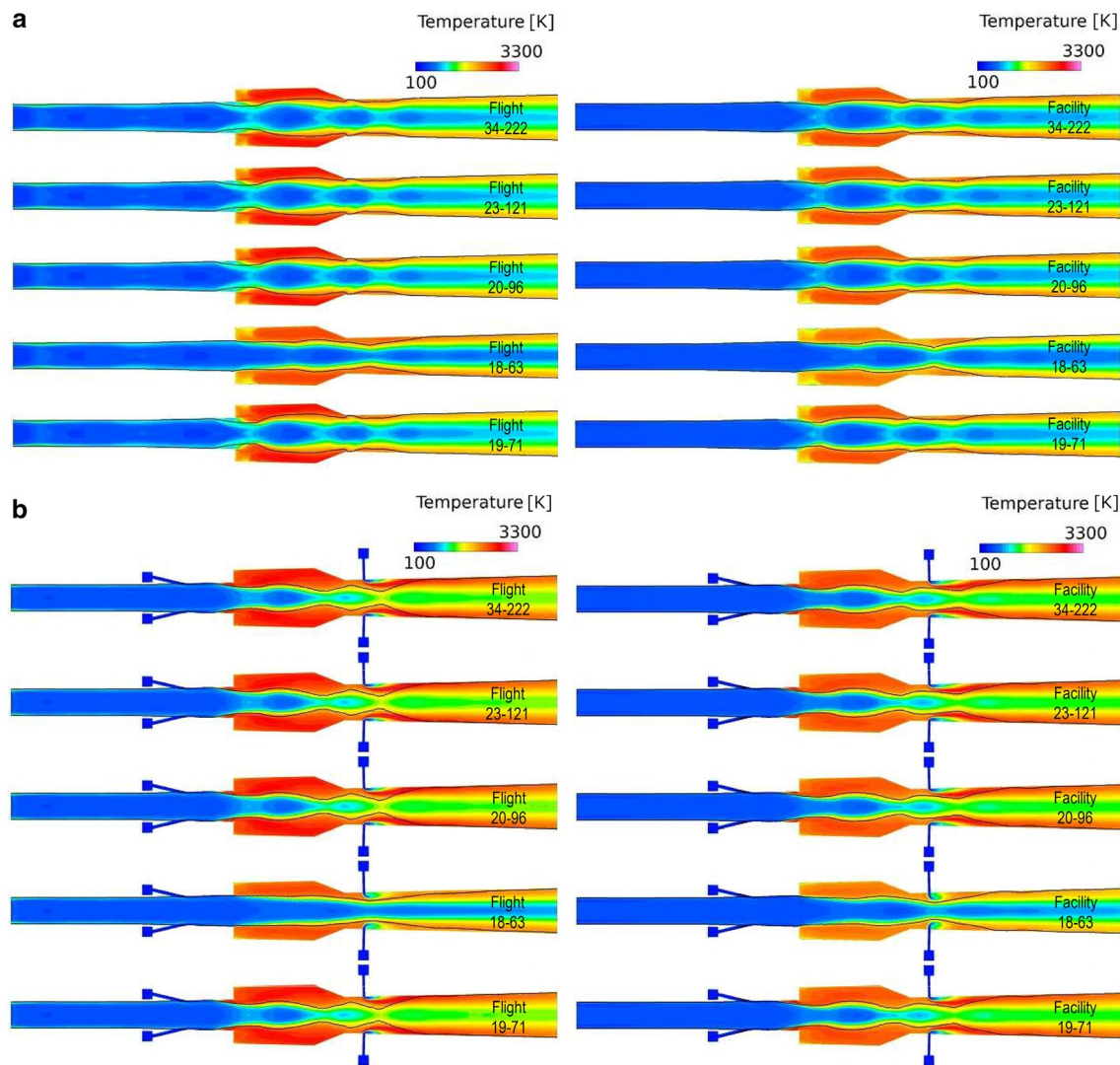


Fig. 18 **a** 2D contour of static temperature in XZ plane at $y=0$ mm for flight (left) and facility (right) conditions. **b** 2D contour of static temperature in XZ plane at $y=12.7$ mm for flight (left) and facility (right) conditions

19–71 models) showed a starting location further upstream than the 18–63 model.

To directly compare the five reaction mechanisms' static temperature distribution, the distributions of the mass flow weighted average values of static temperature are shown in Fig. 19a, b for flight and facility conditions, respectively. In the well-reacted region downstream of the first-stage fuel injection, these two figures showed almost the same features: only the 18–63 model shows a weaker heat release in the first- and second-stage fuel combustion, and the 23–121, 20–96, and 19–71 models reproduce the temperature distribution of the master mechanism (34–222 model) while the 19–71 model slightly overestimates the temperature. The “three-peak” distribution corresponds to the continuous compression (temperature increase) and expansion (temperature decrease) in the core flow, as shown in Fig. 18a, b.

It is also important to focus on the pressure distribution in the simulation results. The static pressure distributions on the sidewall are shown in Fig. 20a (flight conditions) and Fig. 20b (facility conditions). In addition, the static pressure distributions on the top wall are shown in Fig. 21a (flight conditions) and Fig. 21b (facility conditions). Regarding the static pressure distribution in the isolator, there are no peaks for facility conditions, whereas some peaks are observed under flight conditions. This is because the simulation for the facility conditions assumed a direct-connect setup of the facility nozzle and isolator. In contrast, the simulation for the flight conditions was performed from the inlet entrance so that shock waves generated at the inlet enter the isolator under flight conditions. In the well-reacted region downstream of the first-stage fuel injection, the 23–121 and 20–96 models show excellent reproducibility with the target

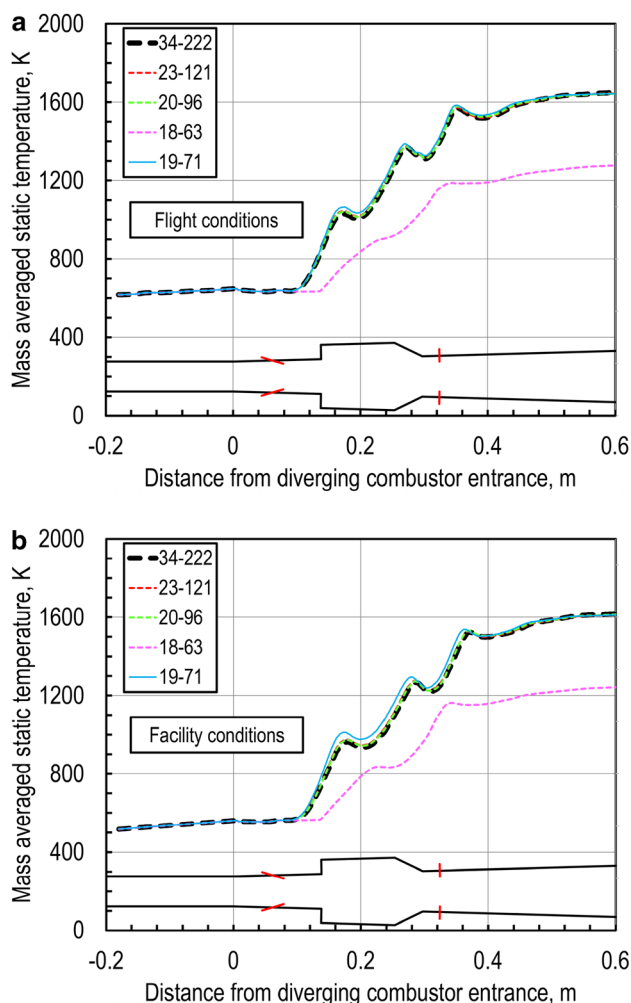


Fig. 19 **a** Master model vs. reduced models for mass averaged static temperature (flight conditions). **b** Master model vs. reduced models for mass averaged static temperature (facility conditions)

mechanism of the 34–222 model. In the 2D simulation, the 19–71 model specificity was pronounced, but the specificity of the 18–63 model was pronounced in 3D simulation as seen in Figs. 17, 18, 19, 20, and 21.

One assumes that a more accurate reaction model with more chemical species would be required to reproduce the higher dimensional phenomena. However, the results of this study show that this is not necessarily the case. The results of the 0D, 1D, 2D, and 3D simulations to this point have yielded an interesting finding: the higher the dimension, the smaller the difference in results among reaction mechanisms. This seems to be because the higher the dimension, the more complicated the reaction regions are distributed in the simulation field. In the 0D ignition delay simulation, for example, the entire simulation region is reactive; the entire cross-section is reactive in the 1D PFR simulation. However, in the 2D slit injection simulation, the reaction region is

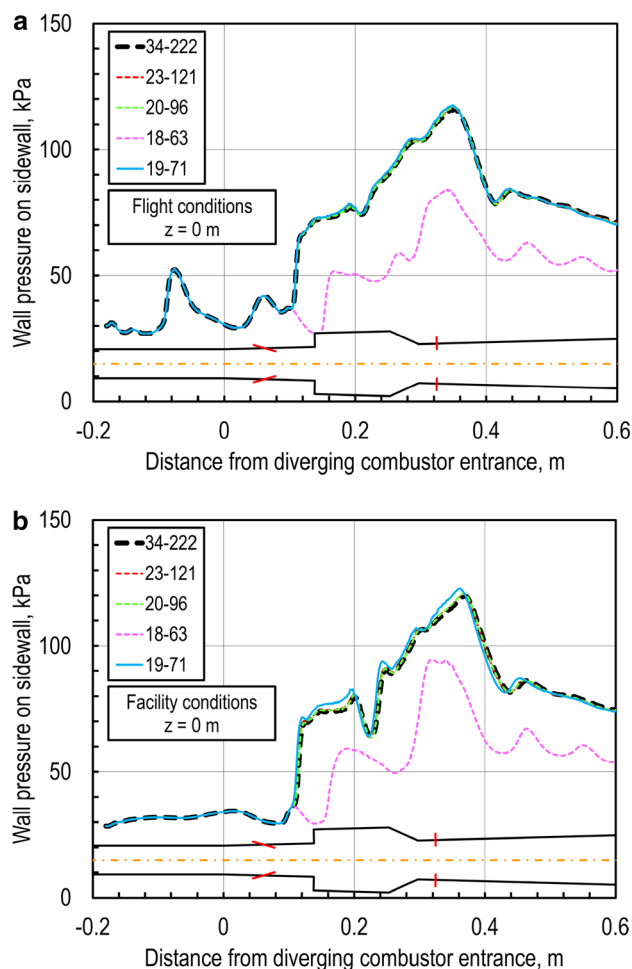


Fig. 20 **a** Master model vs. reduced models for sidewall pressure (flight conditions). **b** Master model vs. reduced models for sidewall pressure (facility conditions)

distributed vertically, and the diffusion flame exists only near the wall. Furthermore, in the 3D combustor simulation, the reaction region is distributed vertically and also spanwise. This important finding shows that the number of chemical species required to reproduce the combustion characteristics in the 3D simulation is lower than expected.

However, there would be the minimum number of chemical species required. For example, the 18–63 model shows lower static pressure and temperature than the other four mechanisms (the 34–222, 23–121, 20–96, and 19–71 models) downstream of the first-stage fuel injector. The difference in chemical species between the 20–96 and 18–63 models are CH_2 and CH_2O , as shown in Table 3. Therefore, there must be the key reaction(s) in 33 (=96–63) elementary reactions, including CH_2 and/or CH_2O . From the observation of the temperature sensitivity of the 33 elementary reactions (although it was in 1D PFR simulation with the 20–96 model by CHEMKIN-Pro), the elementary reactions with CH_2O more strongly affected the temperature

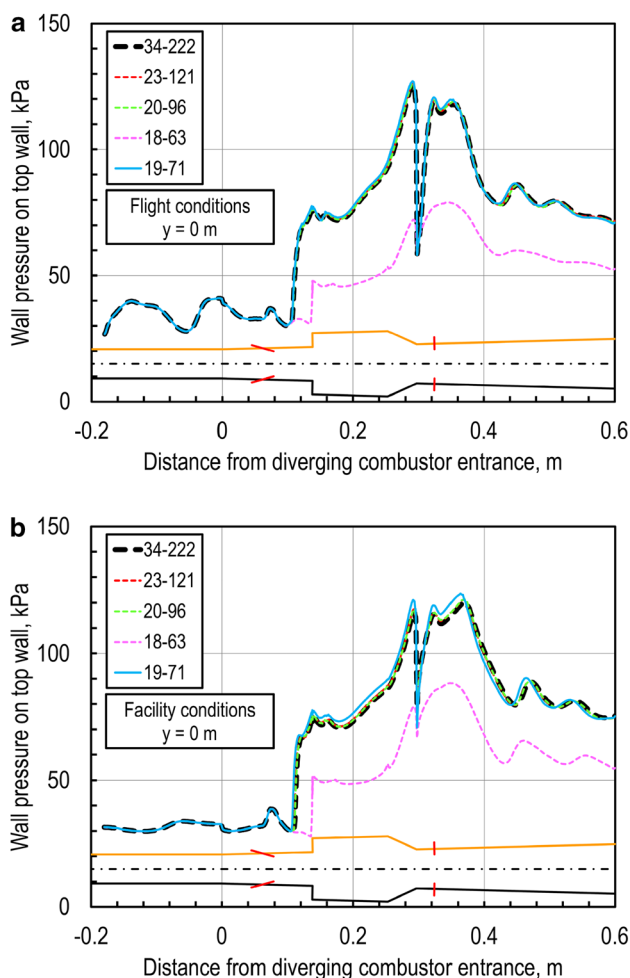


Fig. 21 **a** Master model vs. reduced models for top wall pressure (flight conditions). **b** Master model vs. reduced models for top wall pressure (facility conditions)

than CH_2 . This fact agrees well with the determination of Ref. [28], which experimentally showed the importance of CH_2O in the C_2H_4 combustion process. However, the question remaining is why the result of the 19–71 model shows such excellent agreement with that of the 20–96 and 34–222 models in 3D simulation, although the 19–71 model does not have CH_2O ? According to Table 3, when comparing the 20–96 and 19–71 models, CH_3O , C_2H_2 , and CH_2O are included only in the 20–96 model, and H_2CC and C_2H_5 are included only in the 19–71 model. From these facts, it would be reasonable to assume that the effects of “ CH_3O , C_2H_2 , and CH_2O in the 20–96 model” and “ H_2CC and C_2H_5 in the 19–71 model” on combustion characteristics are comparable.

The effects of the turbulence model and turbulent Schmidt number on the flow field in the simulation are considered. The turbulence model affects eddy viscosity, and the turbulent Schmidt number affects turbulent mixing. Therefore,

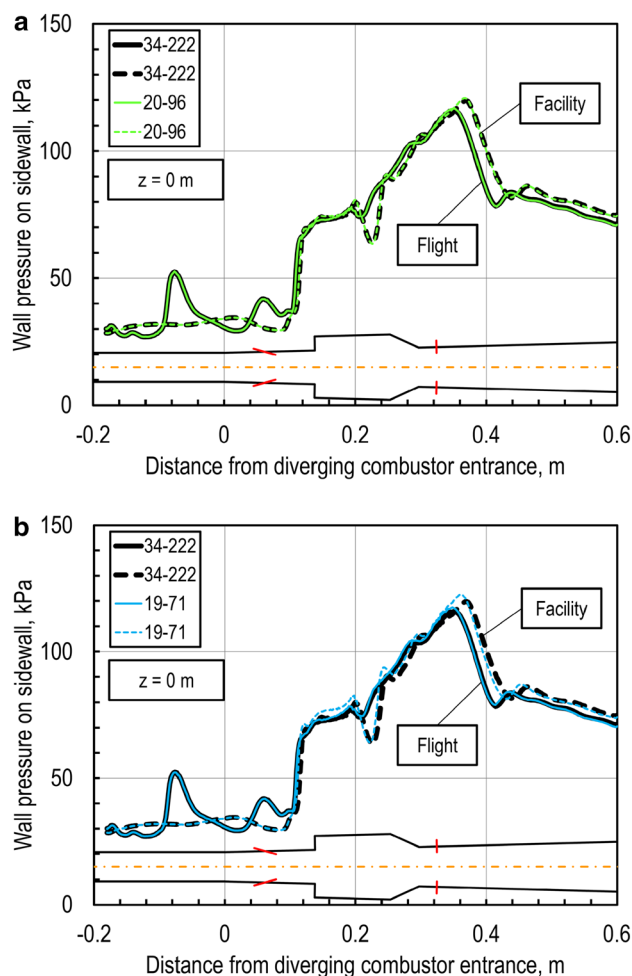


Fig. 22 **a** Master model vs. 20–96 model for sidewall pressure (flight and facility conditions). **b** Master model vs. 19–71 model for sidewall pressure (flight and facility conditions)

the flow field changed when applying a different turbulence model or turbulent Schmidt number. However, the primary objective of the simulation was to compare the combustion characteristics and flow fields of various reaction mechanisms. If the same turbulence model or turbulent Schmidt number is used, the difference in the combustion characteristics and flow field among these reaction models does not change significantly. In other words, even if a different turbulence model or turbulent Schmidt number is used in the simulation, the conclusion obtained in the study would not change.

To conclude this report, let us focus on the most crucial aspect: flight conditions vs. facility conditions in 3D simulations. This project aims to investigate the difference in static pressure distributions in the combustor between flight and facility conditions, and the objective of the study was to obtain an appropriate reduced reaction mechanism to reproduce these two types of static pressure distributions

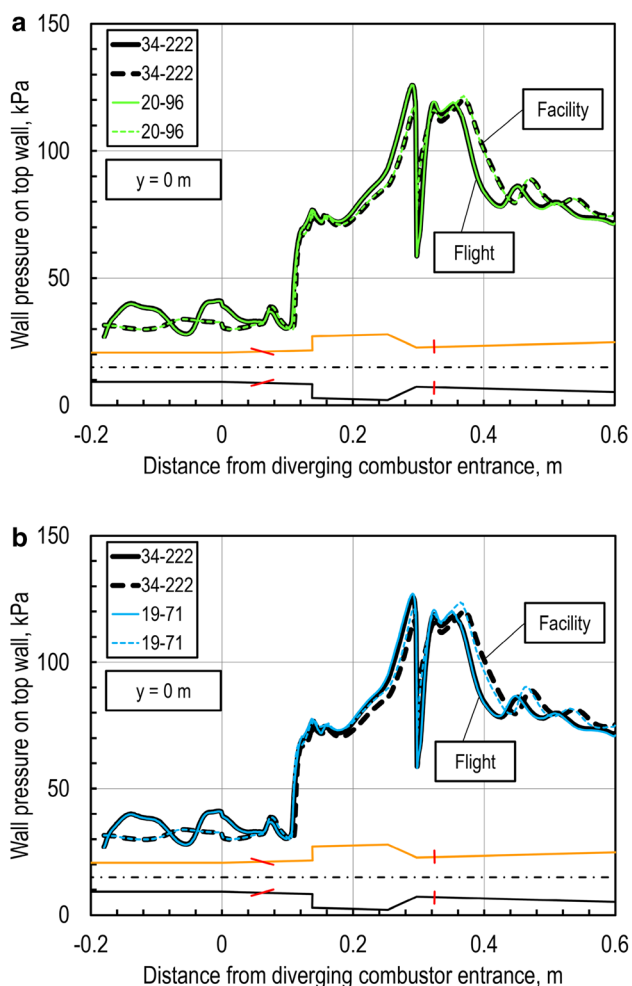


Fig. 23 **a** Master model vs. 20–96 model for top wall pressure (flight and facility conditions). **b** Master model vs. 19–71 model for top wall pressure (flight and facility conditions)

in 3D simulations. Figures 22 and 23 compare flight (solid line) and facility (broken line) conditions for static pressure distributions on the sidewall (Fig. 22) and top wall (Fig. 23). Each figure shows the results of the 34–222 model as the master mechanism and the 20–96 (a) and 19–71 (b) models as candidates for a reduced mechanism.

Regarding the difference in pressure distributions between flight and facility conditions, the peak locations were further downstream for facility conditions. This agrees with that observed in the 2D simulation in the present study and observed in Ref. [2] (although Ref. [2] reported on the H_2 -fueled scramjet). On the other hand, this feature does not agree with that observed in 0D and 1D simulations in the present study. Whether H_2O vitiation in facility conditions promotes or suppresses C_2H_4 combustion is an interesting question. However, the discrepancies observed in the present study indicate that the answer depends on the simulation

target and simulation method examined, and that great care must be taken in discussing this question.

Regarding the reproducibility of the result of the master mechanism, the pressure distributions with the 20–96 model show excellent agreement with those with the 34–222 model under both flight and facility conditions. Therefore, the 20–96 model can reproduce the difference between flight and facility conditions. The pressure distributions with the 19–71 model show excellent agreement with those with the 34–222 model under only flight conditions. As shown in Figs. 22b and 23b, the error in pressure distribution under facility conditions is comparable with the difference in pressure distribution between flight and facility conditions. In addition, the 19–71 model clearly shows different features from other excellent mechanisms in the 0D, 1D, and 2D simulations. So, the 19–71 model would have a greater risk of reaching the wrong conclusion than the 20–96 model. Therefore, the 20-species (96-elementary-reactions) mechanism is recommended as a reduced reaction mechanism for the C_2H_4 -fueled 3D simulation under the flight conditions of the RD1 flight test, which was the focus of this study. The 20-species mechanism consists of H_2 , O_2 , N_2 , H_2O , CO_2 , CO , H , O , OH , HO_2 , CH_2 , CH_2^* , CH_3 , HCO , CH_2O , CH_3O , C_2H_2 , C_2H_3 , C_2H_4 , and CH_2CHO , as shown in Table 3.

7 Conclusion

CHEMKIN-Pro was applied to build a custom-made reduced reaction mechanism suitable for C_2H_4 fueled 3D reacting flow simulation for the JAXA S-520-RD1 flight test project. Reduction of the detailed reaction mechanism (USC Mech II) with 111 species was attempted, aiming to reproduce the static pressure distributions in the diverging combustor. As candidates of reduced mechanism for C_2H_4 /air reaction, the 34-, 23-, 20-, 18-, and 19-species mechanisms were compared with a master mechanism of 111 species. From the results of 0D ignition delay simulation and 1D, 2D, and 3D reacting flow simulations, the 20-species (96-elementary-reactions) mechanism was selected as the best-reduced reaction mechanism for C_2H_4 fueled 3D reacting flow simulation under the flight and facility conditions corresponding to the RD1 flight test. The 20-species mechanism consists of H_2 , O_2 , N_2 , H_2O , CO_2 , CO , H , O , OH , HO_2 , CH_2 , CH_2^* , CH_3 , HCO , CH_2O , CH_3O , C_2H_2 , C_2H_3 , C_2H_4 , and CH_2CHO .

Acknowledgements The authors would like to acknowledge the contributions of T. Shimizu (Japan Aerospace Exploration Agency), J. Aono (Research Center of Computational Mechanics, Inc.), and T. Munakata (Hitachi Solutions East Japan) for their outstanding support of this work. This work was supported by the Innovative Science and Technology Initiative for Security Grant Number JPJ004596, ATLA, Japan.

Data availability The datasets generated and/or analyzed during the current study are available from the corresponding author on reasonable request.

Declarations

Conflict of interest The authors declare that they have no conflicts of interest.

Open Access This article is licensed under a Creative Commons Attribution 4.0 International License, which permits use, sharing, adaptation, distribution and reproduction in any medium or format, as long as you give appropriate credit to the original author(s) and the source, provide a link to the Creative Commons licence, and indicate if changes were made. The images or other third party material in this article are included in the article's Creative Commons licence, unless indicated otherwise in a credit line to the material. If material is not included in the article's Creative Commons licence and your intended use is not permitted by statutory regulation or exceeds the permitted use, you will need to obtain permission directly from the copyright holder. To view a copy of this licence, visit <http://creativecommons.org/licenses/by/4.0/>.

References

- Tani, K., Takegoshi, M., Takasaki, K., Tokudome, S.: JAXA RD1 flight experiment on supersonic combustion, part 1: overview. In: 25th AIAA International Space Planes and Hypersonic Systems and Technologies Conference, Bengaluru, Karnataka, India (2023) **(to be presented)**
- Tomioka, S., Hiraiwa, T., Kobayashi, K., Izumikawa, M., Kishida, T., Yamasaki, H.: Vitiation effects on scramjet engine performance in Mach 6 flight conditions. *J. Prop. Power.* **23**(4), 789–796 (2007)
- Takahashi, M., Kobayashi, K., Takegoshi, M., Saito, T., Onodera, T., Isono, T., Kodera, M., Hasegawa, S., Takasaki, K., Tomioka, S.: JAXA RD1 flight experiment on supersonic combustion, part 2: combustion test result. In: 25th AIAA International Space Planes and Hypersonic Systems and Technologies Conference, Bengaluru, Karnataka, India (2023) **(to be presented)**
- Takahashi, M., Takegoshi, M., Saito, T., Kato, K., Isono, T., Kodera, M., Onodera, T., Tani, K., Kobayashi, K., Tomioka, S.: Post-flight ground tests of an RD1 supersonic combustor model at Mach 6 flight condition. In: 34th International Symposium on Space Technology and Science (ISTS), Kurume, Fukuoka, Japan (2023) **(to be presented)**
- Zambon, A.C., Chelliah, H.K.: Explicit reduced reaction models for ignition, flame propagation, and extinction of $C_2H_4/CH_4/H_2$ and air systems. *Combust. Flame* **150**, 71–91 (2007)
- Mawid, M.A., Sekar, B.: Kinetic modeling of ethylene oxidation in high speed reacting flows. In: 33rd AIAA/ASME/SAE/ASEE Joint Propulsion Conference (JPC), AIAA 97–3269, Seattle, Washington, USA (1997)
- Eklund, D.R., Baurle, R.A., Gruber, M.R.: Numerical study of a scramjet combustor fueled by an aerodynamic ramp injector in dual-mode combustion. In: 39th Aerospace Sciences Meeting (ASM), AIAA 2001–0379, Reno, Nevada, USA (2001)
- Hassan, E., Peterson, D.M., Hagenmaier, M.: Reacting hybrid Reynolds-averaged Navier–Stokes/large-eddy simulation of a supersonic cavity flameholder. In: 52nd AIAA/SAE/ASEE Joint Propulsion Conference (JPC), AIAA 2016–4566, Salt Lake City, Utah, USA (2016)
- CHEMKIN-Pro version 19.2, ANSYS (2019)
- Wang, H., You, X., Joshi, A.V., Davis, S.G., Laskin, A., Egolfopoulos, F., Law, C.K.: USC Mech version II. high-temperature combustion reaction model of $H_2/CO/C_1-C_4$ compounds. http://ignis.usc.edu/USC_Mech_II.htm (2007). Accessed April 2019
- Ogawa, S., Nojima, K., Kobayashi, K., Tomioka, S.: Influence on ignition characteristic by the difference of methane/ethylene mixture gas rate. In: 54th AIAA/SAE/ASEE Joint Propulsion Conference (JPC), AIAA 2018–4777, Cincinnati, Ohio, USA (2018)
- Pepiot-Desjardins, P., Pitsch, H.: An efficient error-propagation-based reduction method for large chemical kinetic mechanisms. *Combust. Flame* **154**(1–2), 67–81 (2008)
- Liang, L., Stevens, J.G., Farrell, J.T.: A dynamic adaptive chemistry scheme for reactive flow computations. *Proc. Combust. Inst.* **32**(1), 527–534 (2009)
- ANSYS Chemkin-Pro Reaction Workbench User's Manual, Release 19.0, ANSYS (2018)
- Liu, Y., Liu, W., Liao, H., Zhou, W., Xu, C.: An experimental and kinetic modelling study on laminar premixed flame characteristics of ethanol/acetone mixtures. *Energies* **14**, 6713 (2021). <https://doi.org/10.3390/en14206713>
- Varatharajan, B., Williams, F.A.: Ethylene ignition and detonation chemistry, part 1: detailed modeling and experimental comparison. *J. Prop. Power.* **18**(2), 344–351 (2002)
- Varatharajan, B., Williams, F.A.: Ethylene ignition and detonation chemistry, part 2: ignition histories and reduced mechanisms. *J. Prop. Power.* **18**(2), 352–362 (2002)
- CRUNCH CFD version 3.3.0, CRAFT Tech (2019)
- Takahashi, M., Tomioka, S., Kodera, M., Kobayashi, K., Hasegawa, S., Shimizu, T., Aono, J., Munakata, T.: Numerical study on combustor flow-path design for a scramjet flight experiment. *Trans. JSASS Aerosp. Tech. Japan* **19**(3), 415–423 (2021)
- Kitamura, K., Fujimoto, K., Shima, E., Kuzuu, K., Wang, Z.J.: Validation of arbitrary unstructured CFD code of aerodynamic analysis. *Trans. Jpn. Soc. Aero. Space Sci.* **53**(182), 311–319 (2011)
- Morii, Y., Terashima, H., Koshi, M., Shimizu, T., Shima, E.: ERENA: a fast and robust Jacobian-free integration method for ordinary differential equations of chemical kinetics. *J. Comp. Phys.* **322**, 547–558 (2016)
- Jameson, A., Yoon, S.: Lower-upper implicit schemes with multiple grids for the Euler equations. *AIAA J.* **25**(7), 929–935 (1987)
- Kitamura, K., Shima, E.: Improvements of simple low-dissipation AUSM against shock instabilities in consideration of interfacial speed of sound. In: 5th European Conference on Computational Fluid Dynamics (ECOMAS CFD 2010), Lisbon, Portugal (2010)
- van Leer, B.: Towards the ultimate conservative difference scheme. V. A second-order sequel to Godunov's method. *J. Comput. Phys.* **32**(1), 101–136 (1979)
- Menter, F.R.: Zonal two equation $k-\omega$ turbulence models for aerodynamic flows. In: AIAA 24th Fluid Dynamics Conference, AIAA 93–2906, Orlando, Florida, USA (1993)
- Georgiadis, N.J., Mankbadi, M.R., Vyas, A.: Turbulence model effects on RANS simulations of the HiFIRE flight 2 ground test configurations. In: 52nd Aerospace Sciences Meeting (ASM), AIAA 2014–0624, National Harbor, Maryland, USA (2014)
- Takahashi, M., Nojima, K., Shimizu, T., Aono, J., Munakata, T.: Numerical simulation of ethylene-fueled scramjet combustor flow by using LS-FLOW solver (comparison of the combustion gas composition). In: Proceedings of 50th fluid dynamics conference/36th aerospace numerical simulation symposium, JAXA-SP-18-005, 159–164 (2019) **(in Japanese)**
- Micka, D.J., Driscoll, J.F.: Stratified jet flames in a heated (1390 K) air cross-flow with autoignition. *Combust. Flame* **159**, 1205–1214 (2012)

Publisher's Note Springer Nature remains neutral with regard to jurisdictional claims in published maps and institutional affiliations.